

Group-Equivariant Diffusion Models for Lattice Field Theory

Octavio Vega ^{1,2*}, Javad Komijani ^{3†}, Aida El-Khadra ^{1,2}, Marina Marinkovic ³

¹*Department of Physics, University of Illinois Urbana-Champaign, Urbana IL 61801*

²*Illinois Center for Advanced Studies of the Universe, University of Illinois
Urbana-Champaign, Urbana IL 61801*

³*Institute for Theoretical Physics, ETH Zürich, 8093 Zürich, Switzerland*

Abstract

Near the critical point, Markov Chain Monte Carlo (MCMC) simulations of lattice quantum field theories (LQFT) become increasingly inefficient due to critical slowing down. In this work, we investigate score-based symmetry-preserving diffusion models as an alternative strategy to sample two-dimensional ϕ^4 and $U(1)$ lattice field theories. We develop score networks that are equivariant to a range of group transformations, including global \mathbb{Z}_2 reflections, local $U(1)$ rotations, and periodic translations \mathbb{T} . The score networks are trained using an augmented training scheme, which significantly improves sample quality in the simulated field theories. We also demonstrate empirically that our symmetry-aware models outperform generic score networks in sample quality, expressivity, and effective sample size.

*octavio5@illinois.edu

†jkomijani@ethz.ch

Contents

1	Introduction	3
2	Building Diffusion Models for LQFT	5
2.1	Diffusion as a Reversible Stochastic Process	5
2.2	Symmetries of Score Functions	8
2.3	Training through Force-Regularized Score Matching	9
2.4	Likelihood Computations and Exactness	10
3	Toy Example in 0D	12
3.1	\mathbb{Z}_2 Symmetry	12
3.2	Training and Inference	14
3.3	Effective Sample Sizes	15
4	Application to Scalar ϕ^4 Theory in 2D	16
4.1	Network Architecture	17
4.2	Numerical Experiments	18
4.3	Influence of Symmetry on Model Expressivity	21
5	Application to U(1) Gauge Theory in 2D	24
5.1	Gauge-Equivariant Score Network	25
5.2	Additional Observables	26
6	Conclusions and Outlook	28
	Acknowledgments	29
A	Lattice Field Theory Formalism	30
A.1	Pure U(1) Lattice Gauge Theory	30
A.2	Derivation of the U(1) Force	31
B	Stochastic Dynamics of Scalar Fields	32
B.1	Derivation of the Fokker-Planck Equation	32
B.2	Reverse Langevin Process	34
B.3	Solving the FP Equation along ODE Trajectories	35
C	Construction of Equivariant Score Networks	35
C.1	Group Symmetries of Score Functions	35
C.2	Discussion on the U(1) Symmetry of Score Functions	38
	References	38

1 Introduction

Lattice Quantum Field Theory (LQFT) provides a non-perturbative avenue for simulating gauge theories via the path integral formalism [82] in Euclidean space-time [6]. In LQFT, Monte Carlo simulation is used to compute expectation values of the observables, which requires averaging over ensembles of field configurations. The efficient sampling of lattice field theories is crucial for non-perturbative studies of fundamental interactions, yet conventional algorithms suffer from poor scalability when approaching the continuum limit [7, 8]. In this paper, we address Monte Carlo techniques in the framework of diffusion models to address the current limitations of standard sampling approaches.

In LQFT with Euclidean action $S[\phi]$, an expectation value of the observable \mathcal{O} is computed with respect to the path integral measure

$$\langle \mathcal{O} \rangle = \frac{1}{\mathcal{Z}} \int \mathcal{D}\phi \mathcal{O}(\phi) e^{-S[\phi]}, \quad (1.1)$$

where \mathcal{Z} is the corresponding Euclidean partition function. The functional integration measure $\mathcal{D}\phi$ represents a sum over all possible configurations, or trajectories, of the dynamical degrees of freedom ϕ . The discretized fields $\phi(x)$ generally live on lattice sites $x \in \mathbb{Z}^{Nd}$. The expectation value (1.1) can be estimated numerically by averaging over batches of samples $\{\phi_i\}_{i=1}^N \sim p[\phi]$ from the probability distribution $p[\phi] = \frac{e^{-S[\phi]}}{\mathcal{Z}}$

$$\langle \mathcal{O} \rangle \approx \frac{1}{N} \sum_{i=1}^N \mathcal{O}(\phi_i). \quad (1.2)$$

The physical distribution $p[\phi]$ can be arbitrarily complicated, often being defined over high-dimensional, multimodal phase spaces. Additionally, the normalization constant \mathcal{Z} is generally intractable. Sampling from such probability densities is, in general, an arduous task that requires carefully tailored sampling algorithms and large computational resources. In LQFT, the ensemble generation stage is generally performed with Markov chain Monte Carlo (MCMC) approaches, e.g. with Metropolis-Hastings [1] or Hybrid-Hamiltonian Monte Carlo (HMC) [2, 3, 4].

Traditional MCMC algorithms suffer from several hindrances that scale poorly with increasing lattice volumes. For instance, autocorrelation times between samples grow very large with decreasing lattice spacing, referred to as *critical slowing down* [5], requiring very long wait times for successive MCMC samples to become decorrelated. The sampling procedure can become stuck within topological sectors [87, 88] and fail to explore the rest of the configuration space— a phenomenon called *topological freezing*. Machine learning (ML) has been widely applied to accelerate various stages of the LQFT simulation pipeline, especially ensemble generation [15, 29, 30].

Generative artificial intelligence (GenAI) has become increasingly popular in its applications to scientific research and high-performance computing. The most current and widely developing instances of GenAI algorithms are deep generative models. There are several classes of generative models with different implementations, capabilities, and limitations, including variational autoencoders (VAE) [35], generative adversarial networks (GAN) [37], and normalizing flows [11, 12, 13].

It has already been established that normalizing flows are capable of probabilistic modeling on complicated geometries [16] as well as sampling of various lattice field theories [17, 18, 19, 20, 21, 22]. Through robust experimentation, progress continues to be made

towards understanding the scalability of flow-based sampling towards the continuum for LQFT [23, 24, 25, 27] and addressing the associated challenges therein [28].

Another promising class of deep generative models that have seen tremendous success in an array of contemporary applications are diffusion models. Drawing from the theory of non-equilibrium thermodynamics, diffusion models frame the training and sampling pipelines through the coupling of a forward (diffusion) process and a reverse (denoising) process, respectively. The inference of new samples is formulated as the solution trajectory to a stochastic differential equation that analytically reverses the forward process [63], viewed simply as evolution under the heat equation. Diffusion models can be viewed alongside normalizing flows through the lens of the Fokker–Planck equation. The former is described by the diffusive component (heat equation) and the latter by the deterministic component (continuity equation). As opposed to learning bijective maps which deterministically transform data, diffusion models learn a reversible stochastic process whose inverse transports ‘diffused’ samples back into posterior samples over time.

Diffusion models have been used with remarkable success for computer vision tasks [50] and high-quality image generation with models such as Imagen [51], GLIDE [52], Stable Diffusion [53], and DALL-E 2 [54]. Another emerging application of diffusion models is to drug discovery and *De Novo* protein design [55, 56], with specific implementations in RFDiffusion [57], DiffInt [58], and DiffDock [59].

Diffusion models have also recently been studied in the context of lattice field theory [67, 69, 70, 71]. The authors of Ref. [68] provide an interesting discussion on the similarities between score-based generation and stochastic quantization [78] for scalar field theories, upon which they expand for Abelian gauge theory in Ref. [77]. It is interesting to explore the efficacy of diffusion-based methods for lattice field theories near phase transitions. Furthermore, the pursuit of diffusion-based sampling for lattice QFT invites further studies of phase transitions and critical behavior with potentially greater efficiency.

In this work, we introduce a new framework for symmetry-preserving diffusion processes for sampling in lattice field theory. We apply our method to two primary examples: scalar field theory and Abelian gauge theory in two spacetime dimensions. The main features of our framework are:

- **Generalized diffusion processes:** We present a novel formalism for stochastic processes which clarifies the role of reversibility in diffusion processes and supports Langevin-based predictor-corrector methods. Our treatment also encompasses both the variance-preserving and variance-expanding pictures of diffusion.
- **Group symmetries of the score:** A key theoretical result derived in this paper is the transformation law of score functions under general group actions, for which we provide a formal proof in Appendix C.1. We discuss this transformation law for several different groups, including the two main examples studied in this paper: \mathbb{Z}_2 and $U(1)$, as well as $SU(N)$. We also provide interpretations of this general result for cases where the underlying data occupies different spaces, such as group manifolds or Lie algebras.
- **Exactly symmetric implementations:** We develop group-equivariant score networks with exact \mathbb{Z}_2 and $U(1)$ equivariance, and partial translation equivariance. Unlike previous approaches relying on approximate symmetry enforcement via data augmentation, our approach enforces symmetry exactly by construction.

- **Force-improved score matching:** We introduce *force-improved score matching* as a new objective function which augments the traditional score matching training procedure by additionally constraining the learned score to match the theory’s force field. This acts as a form of regularization, which corrects the score network at the endpoint of the denoising trajectory and empirically yields higher sample quality in our experiments.

Our paper is organized as follows: in Section 2, we develop the formalism for diffusion processes through stochastic differential equations and discuss our main theoretical result, which is the transformation law for score functions under group symmetries. We further outline the general procedure for training score networks and calculating model likelihoods. Next, in Section 3, we walk through an illustrative example of our pipeline for a \mathbb{Z}_2 -invariant toy theory. This is followed by Section 4, where we present an application of our method to sampling from the ϕ^4 scalar field theory, accompanied by a discussion on the beneficial impact of enforcing symmetries on model quality. In Section 5, we apply our procedure to U(1) gauge theory in 1 + 1 dimensions, and demonstrate the validity of the proposed models by computing the physical observables. We conclude in Section 6 with a summary and discussion of future directions for this work. Our appendices expand on the background and formalism for lattice field theory (Appendix A), stochastic processes (Appendix B), and group symmetries (Appendix C).

2 Building Diffusion Models for LQFT

Diffusion models, originally inspired by non-equilibrium thermodynamics [39], consist of two stochastic processes that evolve data over time. During the first process, called the *forward process*, ground-truth data are “diffused” by random noise until they reach a purely corrupted state where the original signal and its internal correlations are completely erased. After, the *reverse process* progressively undoes the destruction by “denoising” samples from a noisy prior to reconstruct realistic samples. In general, both processes are formulated as continuous-time stochastic processes, but can be simulated through discrete-time Markov chains [40].

In this section, we begin by offering a general formulation of diffusion processes through stochastic differential equations, and explain how they can be reversed. We show how this formalism unifies different frameworks of diffusion models by careful changes of variables. Next, we informally outline our key result that describes how score functions transform equivariantly under group symmetries which leave the action invariant. Then, we outline how score-matching is used to train diffusion models and provide a new addition called *force-regularization* which leverages information about the underlying physical theory. We conclude this section by presenting how model likelihoods are computed to allow for exact calculations.

2.1 Diffusion as a Reversible Stochastic Process

A forward diffusion process can be written as a stochastic differential equation (SDE):

$$d\phi_t = f(\phi_t, t)dt + \sigma dW. \quad (2.1)$$

Here, ϕ_t is the state of the system (or field configuration) at diffusion time t , $f(\phi_t, t)$ represents a deterministic drift term, and dW is the increment of a Wiener process—a

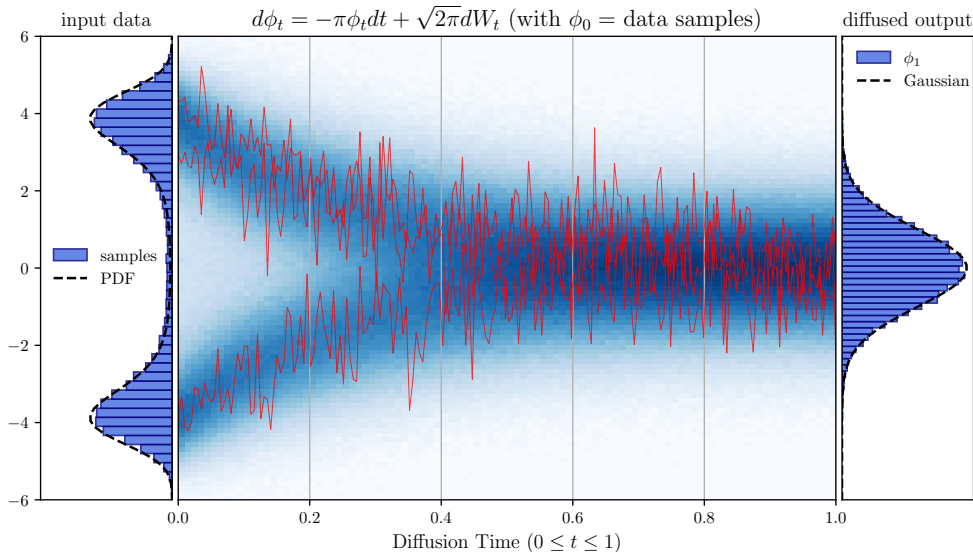


Figure 1: Visualization of the forward diffusion process over time in the variance-preserving picture. The histogram (blue) of data samples is seen to evolve into a Gaussian distribution while the variance is approximately constant in time. The red lines represent three sample trajectories of the data stochastically evolving towards $t = 1$.

Gaussian term of zero mean and variance $|dt|$. In general, σ may also be time-dependent, but we suppress this for now and work with a constant diffusion coefficient.

By setting the drift term to zero, we can define a diffusion model in the framework of machine learning and train it via the algorithms presented in Sec. 2.3. However, a constant σ may require exponentially large time for the diffusion process to lose information about the initial distribution of ϕ_0 . A more efficient approach is to add a non-vanishing drift term $f(\phi_t) = -\gamma\phi_t$ for $\gamma > 0$, which transforms the forward process into

$$d(e^{\gamma t}\phi_t) = \sigma e^{\gamma t}dW. \quad (2.2)$$

This choice accelerates the loss of information while still enabling the use of the same simple algorithms as those employed in the case of vanishing drift.

The solution to the SDE at time $t > 0$ can be expressed in closed form:

$$\phi_t = e^{-\gamma t}\phi_0 + \sigma\sqrt{\frac{1 - e^{-2\gamma t}}{2\gamma}}\epsilon_t, \quad (2.3)$$

where $\epsilon_t \sim \mathcal{N}(0, 1)$. We may set $\sigma = \sqrt{2\gamma}$ so that the variance of ϕ_t approaches 1 at large values of t , i.e., for $t \gg 1/\gamma$. This is an example of *variance-preserving* diffusion processes. Alternatively, one can let σ depend on time (e.g. as $\sigma_0 e^{\gamma t}$) and suppress the drift term. This is called the *variance-expanding* picture, and it is discussed further below.

In Figure 1, we show an example diffusion process evolving according to Eq. (2.2) with $\gamma \equiv \pi$ and $\sigma \equiv \sqrt{2\pi}$. It shows the histogram of samples as time evolves, as well as the trajectories of three samples. The probability density function (PDF) of ϕ_t changes as time evolves from the original distribution at time 0 to a Gaussian-like distributions at time 1. Let us use $p_t(\phi_t; \sigma)$ to denote the PDF of diffused samples at time t . The

evolution of p_t is governed by the Fokker-Planck (FP) equation [60, 61]:

$$\frac{\partial}{\partial t} p_t(\phi_t; \sigma) = \nabla \left(-f(\phi_t, t) + \frac{\sigma^2}{2} \nabla \right) p_t(\phi_t; \sigma). \quad (2.4)$$

For a derivation, see Appendix B.1.

The process in Eq. (2.1) is reversible because the FP equations of the forward and reverse process must be the same. This follows from the fact that a sequential evolution of the random field ϕ governed by equation (2.1) from time t_1 to $t_2 > t_1$ and by an evolution in reverse from t_2 to t_1 does not change the PDF of ϕ . The reverse operation is commonly referred to as a *denoising* process, for which there exists a family of stochastic processes:

$$d\phi_t = f(\phi_t, t)dt - \frac{\sigma^2 + \tilde{\sigma}^2}{2} \nabla \log p_t(\phi_t; \sigma)dt + \tilde{\sigma}dW \quad (2.5)$$

for any real value of $\tilde{\sigma}$. (Similar to σ , $\tilde{\sigma}$ can depend on time, but we drop its time-dependence for simplicity.) We derive this reverse process in Appendix B.2. A common choice is to let $\tilde{\sigma} = \sigma$. Interestingly, when $\tilde{\sigma} = 0$, the denoising process in Eq. (2.5) simplifies to a completely deterministic trajectory called the *probability flow ODE*, which can be interpreted as a continuous normalizing flow [14].

The more general form of the reverse process in (2.5) allows for an intuitive understanding of the sampling process. The reverse SDE can be written as the sum of two terms:

$$d\phi_t = \underbrace{\left(f(\phi_t, t) - \frac{\sigma^2}{2} \nabla \log p_t(\phi_t; \sigma) \right)}_{\text{predictor}} dt + \underbrace{\left(\frac{\tilde{\sigma}^2}{2} \nabla \log p_t(\phi_t; \sigma) |dt| + \tilde{\sigma}dW \right)}_{\text{Langevin corrector}}. \quad (2.6)$$

The first term, labeled *predictor*, plays the role of a deterministic drift, ensuring that samples evolve backwards according to the diffusion process's marginal probabilities. The second term, labeled *Langevin corrector*, has two components that compensate each other; it moves samples towards higher density regions of p_t while also adding random noise in such a way that it preserves the distribution p_t . The preceding explanation holds under the assumption that the samples ϕ_t are indeed drawn from the target distribution $p_t(\phi_t)$. In practice, when the samples are not correctly drawn, e.g. due to discretization effects, the second term can play the role of a corrector that moves the samples towards the correct distribution in the same spirit that the Langevin process works; hence, it is called a Langevin corrector. From this perspective, our reverse SDE intrinsically describes a predictor-corrector sampling scheme [66], where the second term represents a single application of a Langevin corrector at time t .

The apparent asymmetry between Eqs. (2.1) and (2.5) due to the latter's extra drift term can be attributed to the Langevin corrector that does not change under time reversal. Equation (2.6) is written such that it can be applied in both forward and reverse directions; indeed, setting $\tilde{\sigma} = \sigma$ and applying Eq. (2.6) in the forward direction yields the original forward process in Eq. (2.1).

A denoising process aims to recover alternative samples of the original data from the diffused versions by removing the noise that is introduced during the forward diffusion process. A crucial step in applying the denoising process is determining the *score function*, defined as the gradient of $\log p_t(\phi_t)$ with respect to the data:

$$\mathbf{s}(\phi_t, t) := \nabla \log p_t(\phi_t). \quad (2.7)$$

In score-based generative modeling [43], the goal is to learn a neural network approximator for the score function $\hat{\mathbf{s}}_\theta(\phi_t, t) \approx \mathbf{s}(\phi_t, t)$ over time. We discuss how to train score networks in Sec. 2.3. Given a trained score network, the reverse process (2.5) can be solved numerically in reverse time to obtain new samples.

We conclude this section with some remarks on two conventional SDEs used in the literature. The first of these is known as the *variance-preserving* (VP) picture, whose SDE is given by

$$d\phi_t = -\frac{1}{2}\beta(t)\phi_t dt + \sqrt{\beta(t)}dW, \quad (2.8)$$

where $\beta(t)$ is a positive noise schedule. In this framework, the variable ϕ_t evolves with fixed variance, as seen in Fig. 1. This is equivalent to our formulation in Eq. (2.3), where $\beta(t) \equiv 2\gamma$. The second commonly chosen formulation is known as the *variance-expanding* (VE) picture, written as

$$d\phi = \sigma^t dW, \quad (2.9)$$

where σ is some chosen constant that controls the noise level. This process evolves purely by the addition of noise, causing the variance of the variable ϕ_t to explode over time. One can show that, at time t , the variance is

$$\text{Var}[\phi_t] = \frac{\sigma^{2t} - 1}{2 \log \sigma}. \quad (2.10)$$

These two pictures can be unified via a change of variables. Starting with (2.8), we multiply both sides by an integrating factor to obtain

$$e^{\frac{1}{2} \int_0^t \beta(s) ds} \left[d\phi + \frac{1}{2} \beta(t) \phi dt \right] = \sqrt{\beta(t) e^{\int_0^t \beta(s) ds}} dW. \quad (2.11)$$

Simplifying gives

$$d \left[e^{\frac{1}{2} \int_0^t \beta(s) ds} \phi \right] = \sqrt{\frac{d}{dt} \left[e^{\int_0^t \beta(s) ds} \right]} dW, \quad (2.12)$$

which takes exactly the form of a VE SDE with $\sigma^2(t) = e^{\int_0^t \beta(s) ds}$. From this point onward, we use the variance-expanding (VE) scheme for our diffusion processes.

2.2 Symmetries of Score Functions

Many of nature's fundamental interactions are described as consequences of symmetries in the underlying physical theories that describe them. In lattice field theory, we almost always study theories that exhibit one or more symmetries, meaning that the action defining the theory is invariant under some set of transformations: $S[X] = S[g(X)]$. The central ingredient to score-based diffusion models is the score function, derived from the action through differentiation with respect to the field variables. As such, determining the impact these symmetry transformations have on the score function befits the current discussion.

Let $p_t(\phi)$ be some intermediate marginal distribution of a diffusion process and $\mathbf{s}(\phi, t)$ its score function. For lattice field theories, definition 2.7 reduces to the negative gradient of the effective action with respect to the dynamical degrees of freedom:

$$\mathbf{s}(\phi, t) \triangleq -\nabla S_t^{\text{eff}}(\phi), \quad (2.13)$$

which is equivalent to the **force**. Suppose the action is invariant under some group of symmetries \mathcal{G} . For now, we make no assumptions on the nature of the group \mathcal{G} ; we only assume that the representation of its action is smooth. This invites a more abstract interpretation of the result to follow. Let $G \in \mathcal{G}$ be an arbitrary group element and let ρ_G be the representation of the group action on the field ϕ . Then

$$\phi \xrightarrow{G} \phi' = \rho_G(\phi). \quad (2.14)$$

Invariance of the theory means that the action is agnostic to the transformation:

$$S_t(\phi) \mapsto S'_t(\phi') = S_t(\phi). \quad (2.15)$$

Since the action is symmetric, the probability density must remain unchanged under the group action. Because the group action induces a coordinate change on the space of fields, the gradient (score) must transform accordingly. The general transformation law for the score function is

$$\mathbf{s}(\phi, t) \mapsto \mathbf{s}'(\phi', t) = \left(\frac{\partial \rho_G(\phi)}{\partial \phi} \right)^{-\top} \mathbf{s}(\phi, t), \quad (2.16)$$

which we state and prove more formally in Theorem C.4. In summary, the score function, as a covector, generally transforms contravariantly with the Jacobian of the change of variables induced by the group action. How we interpret this result depends on what representation or space the field variables occupy:

- In **linear representations**, the Jacobian is simply the representation matrix R_G , and we recover $\mathbf{s}' = (R_G)^{-\top} \mathbf{s}$.
- For **Lie algebra-valued fields**, the group action acts via the adjoint representation, and the same formula holds with $R_G = \text{Ad}_G$.
- On **curved group manifolds** (e.g. for $\text{SU}(N)$ gauge links), the group acts nonlinearly by conjugation. The differential of this action gives the Jacobian on tangent spaces, and the score, as a gradient, transforms accordingly.

The score function transforms covariantly in the representation dual to the field representation, which, for unitary reps, is often the representation itself. For nonlinear group actions (e.g. conjugation on the group manifold), the Jacobian is a complicated differential, but the *induced group action* on tangent spaces is precisely the adjoint (or bi-adjoint) representation, making the score transform covariantly under the gauge group. In this framework, one can view the score function as *equivariant*.

We provide detailed derivations, formal discussions, and proofs in Appendix C.1. Specific examples of this result applied to \mathbb{Z}_2 in ϕ^4 theory and $\text{U}(1)$ gauge fields can be found in Section 3.1 and Appendix C.2, respectively.

2.3 Training through Force-Regularized Score Matching

Score matching [41] is a technique used to train models to approximate the data distribution $p(\phi)$ by minimizing the difference between the true score $\nabla \log p(\phi)$ and the model

score function $\mathbf{s}_\theta(\phi)$, where θ denotes trainable model parameters. As opposed to minimizing the Kullback-Leiber divergence [42] between the model and target distributions directly, the score matching objective function compares their gradients and is written as

$$J(\theta) = \mathbb{E}_{t \sim \mathcal{U}([0,1])} \mathbb{E}_{\phi_t \sim p_t(\phi_t)} \left[\lambda(t) \|\hat{\mathbf{s}}_\theta(\phi_t, t) - \nabla \log p_t(\phi_t)\|_2^2 \right]. \quad (2.17)$$

To simplify the score matching procedure, it is often more practical to work with the conditional distribution $p_t(\phi_t|\phi_0)$ instead of directly using the marginal distribution $p_t(\phi_t)$. Under mild regularity assumptions, it can be shown that optimizing (2.17) is equivalent to optimizing an alternative objective which only involves the conditional distribution [38], such that the inner expectation is replaced by two nested expectations:

$$\begin{aligned} & \mathbb{E}_{\phi_t \sim p_t(\phi_t)} \left[\|\hat{\mathbf{s}}_\theta(\phi_t, t) - \nabla \log p_t(\phi_t)\|_2^2 \right] \\ & \rightarrow \mathbb{E}_{\phi_0 \sim p(\phi)} \mathbb{E}_{\phi_t \sim p_t(\phi_t|\phi_0)} \left[\|\hat{\mathbf{s}}_\theta(\phi_t, t) - \nabla \log p_t(\phi_t|\phi_0)\|_2^2 \right] + \text{const.} \end{aligned}$$

With this objective, training only requires random sampling from the dataset ($\phi_0 \sim p_0(\phi)$) and the conditional distribution ($\phi_t \sim p_t(\phi_t|\phi_0)$). The rewritten objective function is expressed as a weighted integral over the unit-wide temporal interval $0 \leq t \leq 1$:

$$J(\theta) = \int_0^1 \lambda(t) \mathbb{E}_{\phi_0 \sim p(\phi)} \mathbb{E}_{\phi_t \sim p_t(\phi_t|\phi_0)} \left[\|\hat{\mathbf{s}}_\theta(\phi_t, t) - \nabla \log p_t(\phi_t|\phi_0)\|_2^2 \right] dt. \quad (2.18)$$

The uniform measure with respect to which the outermost expectation is taken is easily sampled; however, computing this expectation value is often memory intensive. In practice, one may sample a time $t \sim \mathcal{U}([0, 1])$ and simply compute the loss at this single time step. This estimate converges to the full loss and provides a faster way of training.

Note that the constant appearing in the above relation is not necessarily finite. To make the loss function finite, an appropriate weight function is needed, for which we choose a simple weight function $\lambda(t) = \sigma(t)^2$ that vanishes as $t \rightarrow 0$. Consequently, training based on this loss function alone gains limited direct insight from the data when $t \ll 1$, relying instead on extrapolation to cover this region. To shift from extrapolation to interpolation, we can incorporate prior knowledge of the score function at $t = 0$ by augmenting the loss function with a regularization term as follows:

$$\mathcal{J}(\theta) = J(\theta) + c_0 \mathbb{E}_{\phi_0 \sim p_0(\phi_0)} \left[\|\hat{\mathbf{s}}_\theta(\phi_0, 0) + \nabla S[\phi_0]\|_2^2 \right], \quad (2.19)$$

where $c_0 \geq 0$ is a regularization coefficient. Although this augmentation may not be useful for many applications of diffusion models, it can be readily applied in lattice field theory, where $\partial_{\phi_0} \log p_0(\phi_0)$ (the force) is analytically known. We summarize our training procedure in Algorithm 1.

2.4 Likelihood Computations and Exactness

Generative models for lattice field theory must be **exact**, meaning that generated samples must be asymptotically distributed according to the target distribution. Machine learning models are always biased, but the discrepancy between learned and target probabilities can be corrected given that the model probability of samples $q(\phi)$ can be computed.

In principle, the model log-likelihood of generated samples can be computed simultaneously as samples are generated. To illustrate, consider evolving backwards in time by a small step size h :

$$\begin{pmatrix} \phi_t \\ \log q_t(\phi_t) \end{pmatrix} \rightarrow \begin{pmatrix} \phi_{t-h} \\ \log q_{t-h}(\phi_{t-h}) \end{pmatrix} \quad (2.20)$$

Algorithm 1 Force-Regularized Training

```

1: Input: Training data  $\Phi_0$ , variance function  $\sigma_t$ , neural net  $\mathbf{s}_\theta$ , action  $S$ 
2: Initialize: Parameters of model  $\theta$ 
3: for each epoch do
4:   Loss  $\leftarrow 0$ 
5:   for each minibatch  $\{\phi_0\} \subseteq \Phi_0$  do
6:     Sample  $t \sim \mathcal{U}([0, 1])$  for each config
7:     Sample  $\epsilon \sim \mathcal{N}(0, \mathbf{1})$  for each config
8:      $\phi_t = \phi_0 + \sigma_t \epsilon$  // diffuse data (VE)
9:      $\mathcal{J}(\theta) = \|\sigma_t \mathbf{s}_\theta(\phi_t, t) + \epsilon\|_2^2 + c_0 \|\mathbf{s}_\theta(\phi_0, 0) + S'(\phi_0)\|_2^2$  // estimate loss
10:    Loss  $\leftarrow \mathcal{J}(\theta) + \text{Loss}$ 
11:    Compute gradient:  $\nabla_\theta \text{Loss}$ 
12:    Update parameters  $\theta$  with Adam
13: return  $\hat{\mathbf{s}}_\theta$ 

```

Then, as discussed previously, the sample evolves first by a deterministic drift, and is then corrected by an extra term involving noise:

$$\phi_t \xrightarrow[\text{predictor}]{-h \left[f(\phi_t, t) - \frac{\sigma^2}{2} \mathbf{s}(\phi_t, t) \right]} \phi'_{t-h} \xrightarrow[\text{corrector}]{+h \frac{\tilde{\sigma}^2}{2} \mathbf{s}(\phi_t, t) + \sqrt{h} \tilde{\sigma} \eta_t} \phi_{t-h} \quad (2.21)$$

The corrector step shifts the sample to another sample also distributed according to the same marginal density via

$$\phi'_{t-h} \rightarrow \phi_{t-h} = \underbrace{\phi'_{t-h} - h \frac{\tilde{\sigma}^2}{2} \mathbf{s}(\phi_t, t) + \sqrt{h} \tilde{\sigma} \eta_t}_{\Delta \phi}. \quad (2.22)$$

The drift term evolves ϕ_t according to the probability flow ODE, along which $\log q_t$ evolves accordingly. However, the corrector step induces an extra discretization error:

$$\log q_t(\phi_t + \Delta \phi) = \log q_t(\phi_t) + \mathbf{s}(\phi_t, t) \Delta \phi + O((\Delta \phi)^2). \quad (2.23)$$

In our framework, the step size can be effectively controlled by the parameter $\tilde{\sigma}$ which is decoupled from the step size h and the forward noise σ . In practice, it is common to see only the probability flow ODE ($\tilde{\sigma} = 0$) used for generation when computing model likelihoods to avoid compounding discretization effects.

Assuming a variable ϕ_t evolves according to (2.1), then Eq. (2.4) can be used to solve an ODE for $\log q_t$ along deterministic trajectories in reverse time, which results in

$$\log q_0(\phi_0) = \log q_1(\phi_1) + \int_0^1 \nabla \cdot \mathbf{f}_\theta(\phi_t, t) dt, \quad (2.24)$$

where

$$\mathbf{f}_\theta(\phi_t, t) := f(\phi_t, t) - \frac{\sigma^2}{2} \hat{\mathbf{s}}_\theta(\phi_t, t). \quad (2.25)$$

We provide the argument for this solution in Appendix B.3. In general, computing the divergence term inside the integrand of (2.24) is intractable; however, one can make use of the *Skilling-Hutchinson trace estimator* [89, 90]

$$\nabla \cdot \mathbf{f}_\theta \triangleq \text{Tr} [J_{\mathbf{f}_\theta}] = \mathbb{E}_{\epsilon \sim \mathcal{N}(0, \mathbf{1})} [\epsilon^\top J_{\mathbf{f}_\theta} \epsilon]. \quad (2.26)$$

to obtain an unbiased estimate for the divergence.

Equipped with the ability to compute model probabilities, one gains access to two avenues for ensuring exactness in downstream calculations, which we briefly detail here:

- **Reweighting:** A change of probability measure allows one to reweight [31] their observables directly inside the expectation:

$$\langle \mathcal{O}(\phi) \rangle_p = \left\langle \mathcal{O}(\phi) \frac{p(\phi)}{q(\phi)} \right\rangle_q. \quad (2.27)$$

- **Resampling:** By resampling a generated ensemble with an accept / reject step, one can construct an asymptotically exact Markov chain with an acceptance probability given by

$$A(\phi'|\phi) = \min \left(1, \frac{p(\phi')q(\phi)}{q(\phi')p(\phi)} \right). \quad (2.28)$$

The method one chooses to perform exact calculations depends on how efficient drawing samples from a trained model is compared to computing observables.

3 Toy Example in 0D

In this section, we illustrate the pipeline of equivariant score-based generative modeling with our symmetric diffusion models using a simple example involving a univariate probability density.

3.1 \mathbb{Z}_2 Symmetry

We define a toy theory on a zero-dimensional lattice through the action

$$S(\phi) = \frac{1}{2}m^2\phi^2 + \frac{\lambda}{4!}\phi^4, \quad (3.1)$$

where the variable ϕ corresponds to one dynamical degree of freedom occupying a single lattice site. Notably, this theory exhibits two distinct phases that depend on the action parameters:

- *symmetric phase:* $\frac{\lambda}{m^2} > 0$ (single well potential)
- *broken phase:* $\frac{\lambda}{m^2} < 0$ (double well potential)

which correspond to the topological phases of the model. In this example, we explore both phases by choosing the following action parameters: $m^2 = \pm 1.0$, $\lambda = 0.4$.

This toy model is clearly \mathbb{Z}_2 -invariant, since the action (3.1) enjoys the discrete global symmetry $S(-\phi) = S(\phi)$ under $\phi \mapsto -\phi$. This means that the samples, modulo random statistical fluctuations, should be distributed symmetrically about $\phi = 0$. This is in accordance with the general result, derived in Sec. 2.2; in the case where $\mathcal{G} = \mathbb{Z}_2$, then clearly $\rho(\phi) = -\phi$, so (C.10) reduces to

$$\mathbf{s}(\phi, t) \mapsto -\mathbf{s}(\phi, t). \quad (3.2)$$

In other words, the score function for a zero-dimensional scalar field theory with global \mathbb{Z}_2 invariance is, in turn, \mathbb{Z}_2 -equivariant. The \mathbb{Z}_2 symmetry of Eq. (3.1) is explicit when computing the force:

$$-\frac{\partial S(\phi)}{\partial \phi} = -m^2\phi - \frac{\lambda}{3!}\phi^3, \quad (3.3)$$

which is clearly odd in ϕ . This inspires us to construct a score network which is also \mathbb{Z}_2 -equivariant such that the diffusion model need not learn this discrete symmetry of the theory, but is endowed with it instead.

For our score network, we use a simple multilayer perceptron (MLP) with a custom-built antisymmetric sigmoidal activation function, defined in terms of the usual sigmoid function $\sigma(z)$ as

$$\text{OddSigmoid}(z) := \frac{1}{2} - \frac{e^{-z}}{1 + e^{-z}} = \sigma(z) - \frac{1}{2}. \quad (3.4)$$

The manifest symmetry in the MLP score networks is displayed in Fig. 2. Since the

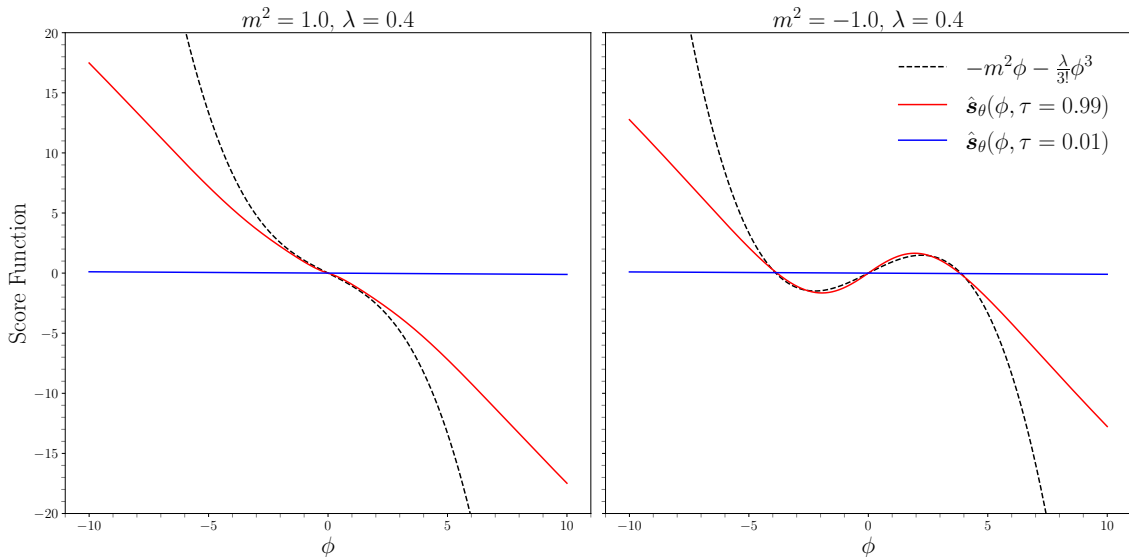


Figure 2: Learned scores as functions of the field variable ϕ in the (left) symmetric and (right) broken phases. The blue and red solid lines correspond to the score functions near the start ($\tau = 0.01$) and end ($\tau = 0.99$) of the reverse process, respectively. The dotted black line represents the true force, i.e. $-\nabla_{\phi}S(\phi)$.

score function must learn to denoise data ϕ_t conditioned on time t , the score network must also be time-dependent. The raw input time would be a scalar $t \in (0, 1)$, but to properly condition a neural network, a more expressive representation is needed. In score-based diffusion models, the general practice is to lift t into a higher-dimensional space through a process called *time embedding*. Different methods exist for embedding sequential information, for instance, sinusoidal positional encodings [32] or Gaussian Fourier projections [33].

Diffusion time is a continuous variable, of which diffusion models must learn complex time-dependent score functions. In light of this, we choose to encode time via Gaussian Fourier embeddings, where random frequencies f_i are chosen from a Gaussian distribution and fixed according to a predefined embedding dimension d . Then the embedding is built as

$$t \mapsto [\sin(2\pi f_1 t), \cos(2\pi f_1 t), \dots, \sin(2\pi f_d t), \cos(2\pi f_d t)]. \quad (3.5)$$

Projecting times into a random, higher-dimensional Fourier basis improves the universal function approximation capacity of the model to learn arbitrary smooth functions of time. This method of time embedding in diffusion models is seen to perform better than the geometric progression of frequencies in sinusoidal positional embeddings [46].

3.2 Training and Inference

For training, we use HMC to prepare ensembles of size 16,384 in both the single and double well phases. We train the diffusion models in this example with the Adam optimizer [36] for 250 epochs with a learning rate of 0.0001 and batch sizes of 256. The training proceeds as outlined in Algorithm 1.

For inference, we generate new samples by solving the reverse ODE using a numerical Euler integrator with a step size of 0.002 (500 time steps). In order to illustrate sample quality, we also employ a similar Euler-Maruyama integrator to solve the reverse SDE, noting that likelihood calculation is best performed in tandem with deterministic generation. We display samples from our trained models compared to the HMC data on which they were trained for both phases in Fig. 3.

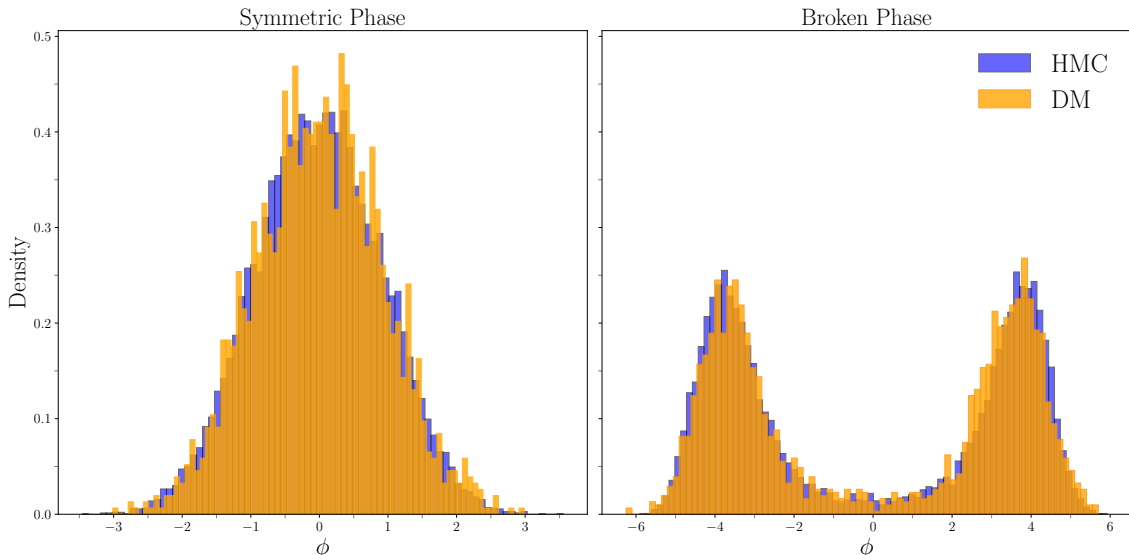


Figure 3: Normalized histograms with 80 bins over 16,384 samples of training data (HMC) and 2,048 samples of diffusion model (DM) generated data for (left) the symmetric and (right) broken phases. The coupling strength was set to $\lambda = 0.4$ for both phases, and the squared mass is $m^2 = 1.0$ and $m^2 = -1.0$ for the two phases, respectively.

As shown in Figure 2, the models learn the score functions very well within regions of ϕ centered around the local minima (wells), since these correspond to areas of high probability. The regions beyond the middle zone where the score network seems to fail to learn the force accurately correspond to areas of much lower likelihood, meaning much fewer samples of data exist there. Because they are manifestly odd in ϕ and must therefore vanish at $\phi = 0$, the models approximate the score functions well near $\phi = 0$. Non-odd score networks are also capable of good performance, though we prefer to work with \mathbb{Z}_2 -equivariant networks in order to exactly replicate the theory’s symmetry and because we observe higher sample quality with symmetric networks.

At each intermediate time step $\tau \in [0, 1]$ along the reverse diffusion process, the learned score function defines, up to additive constants, an effective action $S_\tau^{\text{eff}}(\phi)$ corresponding to the learned density at that time. For this simple 1-dimensional example, the effective action can be easily computed and visualized by cumulatively integrating the learned score functions with respect to ϕ over fixed intervals $[\phi_{\min}, \phi_{\max}] \subset \mathbb{R}$:

$$S_\tau^{\text{eff}}(\phi) = \int_{\phi_{\min}}^{\phi} \hat{\mathbf{s}}_\theta(\tilde{\phi}, \tau) d\tilde{\phi}. \quad (3.6)$$

To illustrate, we plot the trajectory of learned effective actions for the broken phase in Fig. 4. Through the effective action $S_\tau^{\text{eff}}(\phi) := -\log q_\tau(\phi)$, the learned score function also

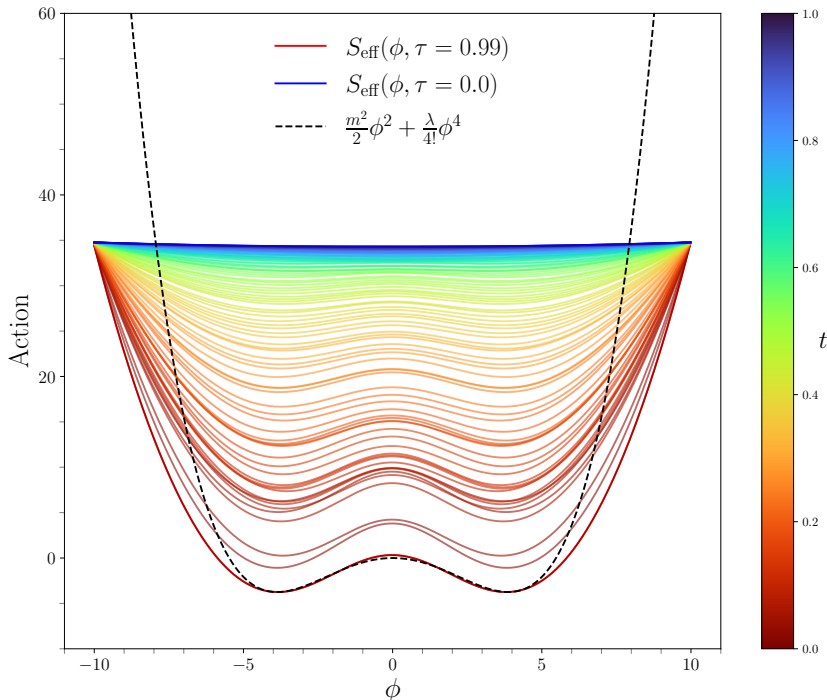


Figure 4: Evolution of the effective action in the broken phase as a function of the field ϕ over reverse diffusion time. The colorbar is parameterized by (forward) diffusion time $t \equiv 1 - \tau$.

implicitly defines (up to normalization) an effective probability density of the generated samples at any point τ in the reverse process. More visualization of the learned effective actions along with their approximate densities over diffusion time τ and the field ϕ are seen in Fig. 5.

3.3 Effective Sample Sizes

At this point, given the ease of interpretation of this toy example, we review the concept of effective sample size (ESS). Given a target distribution p and a model distribution q , the ESS is defined as

$$\text{ESS} := \frac{\left(\frac{1}{N} \sum_{i=1}^N p[\phi_i] / q[\phi_i] \right)^2}{\frac{1}{N} \sum_{i=1}^N (p[\phi_i] / q[\phi_i])^2}, \quad (3.7)$$

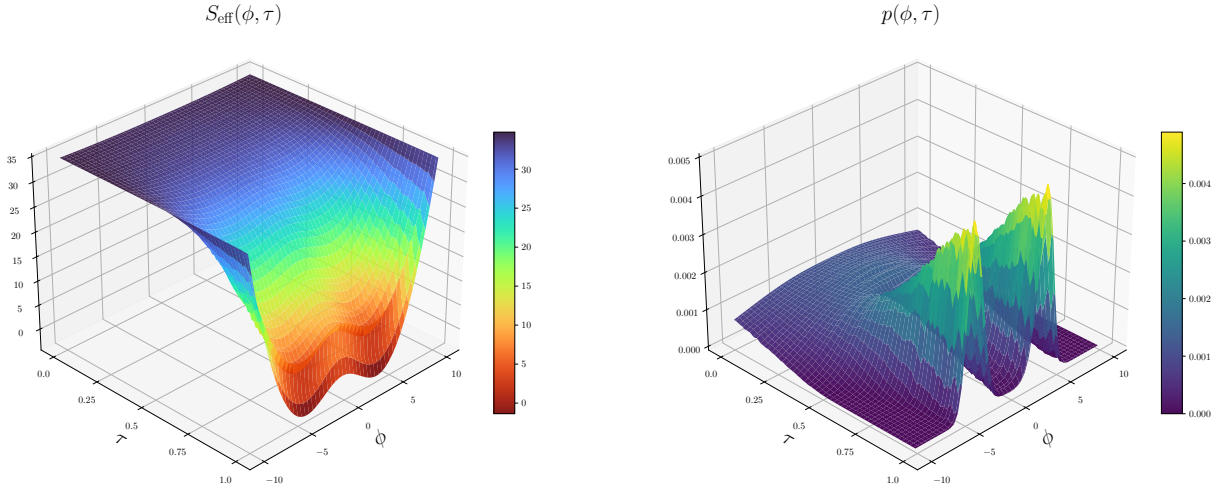


Figure 5: Evolution of (left) the effective action $S_{\text{eff}}(\phi, t)$ and (right) the resulting density $p(\phi, t) \propto e^{-S_{\text{eff}}(\phi, t)}$ over reverse diffusion time τ as a function of the field ϕ .

where N is the number of samples in an ensemble of configurations $\{\phi_i\}_{i=1}^N$. Given that the target distribution is defined by a physical action $S[\phi] =: -\log p[\phi]$ and the model likelihood induces an effective action $S_{\text{eff}}[\phi] := -\log q[\phi]$, Eq. (3.7) can also be written as

$$\text{ESS} = \frac{\left(\frac{1}{N} \sum_{i=1}^N w(\phi_i)\right)^2}{\frac{1}{N} \sum_{i=1}^N w(\phi_i)^2}, \quad (3.8)$$

where the $w(\phi_i)$ represent weighting factors given by

$$w(\phi_i) = \exp(-S[\phi_i] + S_{\text{eff}}[\phi_i]). \quad (3.9)$$

These weighting factors allow us to reframe the discussion in the context of importance sampling, where samples from q are used to approximate expectations under p :

$$\mathbb{E}_p[\mathcal{O}(\phi)] = \int \mathcal{D}\phi \mathcal{O}(\phi) p[\phi] = \int \mathcal{D}\phi \mathcal{O}(\phi) w(\phi) q[\phi]. \quad (3.10)$$

When the weights $w_i \equiv w(\phi_i)$ are very uneven, i.e. in the case where a few samples contribute very large weights that dominate, then this estimate becomes poor, resulting in an effective number of samples much smaller than the total number N . In this way, we view the ESS as the fraction of the generated configurations which are statistically useful. Furthermore, the ESS takes values in $[0, 1]$, where $\text{ESS} = 1$ corresponds to a perfect model where all generated configurations are weighted equally and are truly i.i.d. from the target. We obtain effective sample sizes of **99.4%** and **94.6%** in the symmetric and broken phases, respectively.

4 Application to Scalar ϕ^4 Theory in 2D

The scalar ϕ^4 theory is often referred to as the simplest interacting quantum field theory that still captures many of the key nontrivial features of more complex theories. That such rich behavior can be studied from such a simply written theory makes the ϕ^4 model a powerful testbed. For example, many systems near critical points in statistical field

theory behave like the ϕ^4 theory [84]. This makes it a prototype for phase transitions and studying universality. From the lens of renormalization, the ϕ^4 theory is also simple enough for explorations of RG flow, UV divergences, and other concepts in effective field theory [85].

The ϕ^4 theory is also an important playground for studying non-perturbative dynamics on the lattice, including spontaneous symmetry breaking and triviality in 4D [80]. It is also a very relevant testbed for algorithm development, as many lattice algorithms are first tested on ϕ^4 before being applied to more complex theories [79]. In this section, we continue this tradition by developing and applying diffusion models to the scalar ϕ^4 theory in two spacetime dimensions.

The lattice action for the scalar ϕ^4 theory can be written as

$$S[\phi] = \sum_x \left[-\kappa \sum_{\mu} \phi(x)\phi(x + \hat{\mu}) + (1 - 2\lambda) \phi(x)^2 + \lambda\phi(x)^4 \right], \quad (4.1)$$

which, in addition to the local potential terms from the zero-dimensional example, now includes extended nearest-neighbor interaction terms that allow the field to propagate through spacetime. Notably, (4.1) exhibits a global \mathbb{Z}_2 invariance as well, meaning that its force- and therefore the score function- should be \mathbb{Z}_2 -equivariant following the discussion in Section 3.1.

4.1 Network Architecture

We borrow a well-known architecture from computer vision applications, known as the U-Net, which was first used for semantic segmentation in biomedical imaging [34]. The U-Net consists of two sequential components: a contracting (encoding) path and an expanding (decoding) path, to which its name is owed. The encoder consists of several convolutional layers which gradually downsample the input image while increasing the number of channels; afterwards, the decoder upsamples the image again using transposed convolutions while simultaneously decreasing the number of channels back down to 1. Additionally, residual (skip) connections in the network concatenate data in the decoder with the intermediate data from the encoding path at the same spatial resolution.

In Fig. 6, we display an example diagram of our U-Net architecture that showcases how the lattice geometry evolves as it moves through the network. In each convolutional block, a convolutional layer is applied which preserves the data’s dimensions while increasing the number of channels. This is followed by the application of a group normalization layer and another convolutional layer which downsamples the lattice by a factor of two in each direction. In the expanding path, we use transposed convolutions to restore the spatial resolution of the data.

In two spatial dimensions, scalar field configurations can be thought of as images; here, the ‘pixels’ correspond to the field values at each of the corresponding lattice sites $\phi(x) \in (-\infty, \infty)$, and the image width/height are the spatial lattice extents $L \times L$. Similarly, instead of RGB channels, we have a single channel. Unlike images, however, field configurations and the lattices on which they reside are endowed with certain physical symmetries, which we show can be built in to score-based diffusion models via the design of the score network itself. In Sec. 4.3, we detail the beneficial impact that respecting these symmetries has on our model quality.

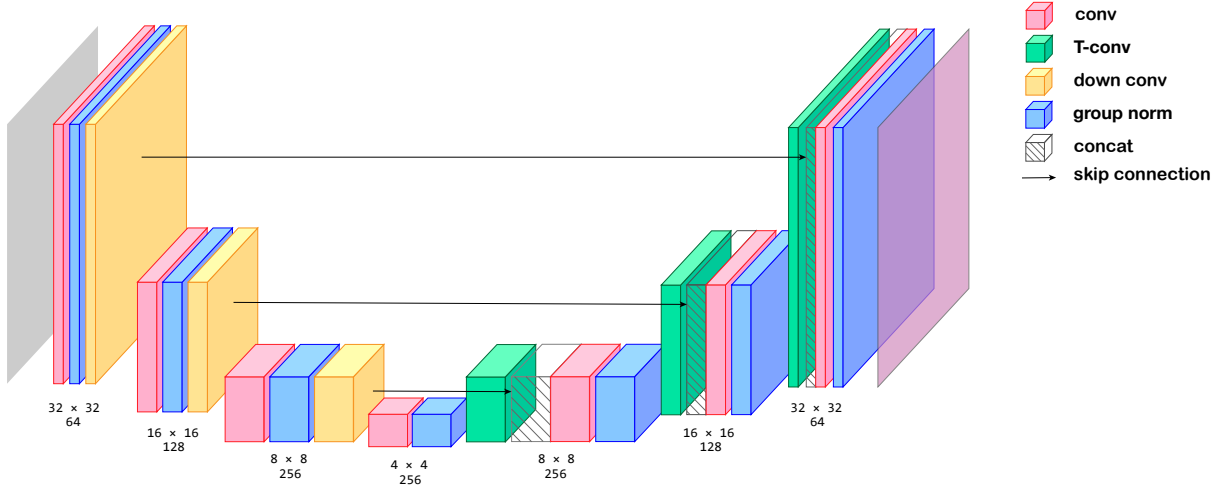


Figure 6: Schematic of U-Net architecture used in our experiments to parameterize the score network, in the example of a 32×32 input. At each stage, convolutional blocks downsample the resolution of the configurations while increasing the intermediate channels, after which transposed convolutions perform the reverse operation. Beneath each convolutional block, the top pair of numbers represents the shape of the data at that resolution and the bottom number is the corresponding number of channels. The input and output are assumed to have a single channel, and are shaped $(\cdot, 1, L, L)$.

Our current implementation of a \mathbb{Z}_2 -equivariant network is to take a generic (non-equivariant) U-Net and anti-symmetrize it:

$$\bar{\mathbf{s}}_{\theta}(\phi, t) = \frac{1}{2}(\hat{\mathbf{s}}_{\theta}(\phi, t) - \hat{\mathbf{s}}_{\theta}(-\phi, t)) \quad (4.2)$$

such that the resulting score function $\bar{\mathbf{s}}_{\theta}$ is odd by construction. This enables us to use a conventional, unrestricted implementation of a U-Net (with circularly padded convolutional layers and SiLU activation functions) to parameterize a still \mathbb{Z}_2 -equivariant score. In practice, this requires twice as many score network evaluations during inference. In principle, such a \mathbb{Z}_2 -equivariant U-Net can alternatively be constructed by using layers which respect this symmetry and odd activation functions, as we did in Section 3.1.

The theory also respects an important spacetime symmetry. Namely, in LQFT simulations, the lattices obey *periodic boundary conditions* as a means of replicating an infinite spacetime continuum while avoiding edge artifacts. As such, respecting the toroidal boundary conditions of lattice configurations should also be taken into consideration. To do so, we use *circular padding* in the convolutional layers of our score network. Our numerical experiments demonstrate that incorporating this explicitly, as opposed to using traditional padding, greatly enhances model quality.

4.2 Numerical Experiments

For all of our experiments, we focus on the broken phase, where $\frac{\lambda}{m^2} < 0$. The specific parameters we choose are $m^2 = -2.68$, $\lambda = 0.5$, $\kappa = 0.67$, which we choose because they correspond to the broken phase, but not overly far from the critical point so that we will see non-trivial behavior. Our training dataset consists of 16,384 configurations which were generated in parallel using 200 HMC iterations with hot initialization. Each

HMC iteration contains 20 leapfrog steps of step size 0.05 so that each trajectory has unit length. We train for 250 epochs with a batch size of 128 at a learning rate of 0.0001.

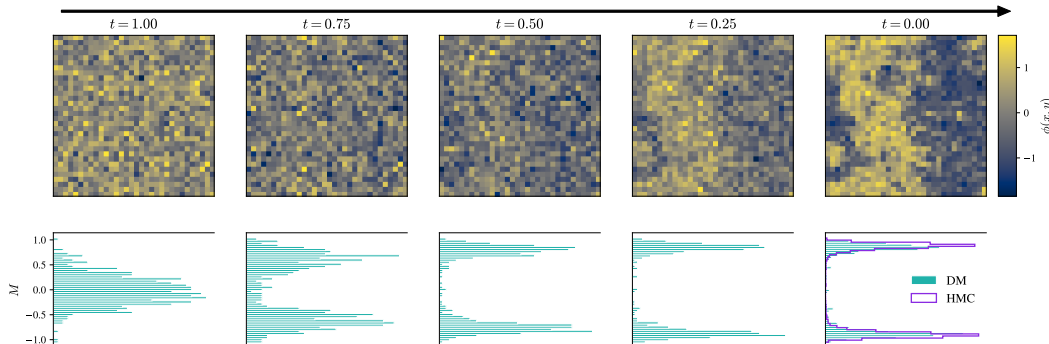


Figure 7: The top row pictures a sample ϕ^4 configuration deep in the broken phase on an 32×32 lattice evolving over reverse diffusion time from left to right. The sample progresses from pure noise to a realistic configuration with local correlations. The bottom row displays the evolution of the magnetization (M) histograms over reverse diffusion time, and the last panel compares the resulting diffusion model (DM) density with the density computed on an HMC-generated dataset. This 32×32 example is meant as illustration to provide a higher resolution image, but our numerical experiments in this section focus on 8×8 lattices.

For inference, we use a fourth order Runge-Kutta integrator [64, 65] to solve the probability flow ODE with a step size of 0.002 (500 time steps) to generate new samples ϕ . We simultaneously solve the probability flow ODE for the model log-likelihood $\log q[\phi]$ using the Skilling-Hutchinson estimator with 10 random Rademacher [91] vectors for the divergence estimate. Together, the backwards process amounts to solving the following system of ODEs:

$$\frac{d}{dt} \begin{pmatrix} \phi_t \\ \log q_t[\phi_t] \end{pmatrix} = - \begin{pmatrix} \frac{1}{2} \sigma^{2t} \hat{\mathbf{s}}_\theta(\phi_t, t) \\ \nabla \cdot [\sigma^{2t} \hat{\mathbf{s}}_\theta(\phi_t, t)] \end{pmatrix}. \quad (4.3)$$

We quantitatively validate our models by computing physically relevant quantities and comparing them either to previously-existing estimates computed on Monte Carlo data, their exactly known values (when available), or both. We focus on the following physical observables relevant to the ϕ^4 theory for validation (where $V = L^2$ denotes the lattice volume):

- Magnetization (mean-field value):

$$M = \frac{1}{V} \sum_x \phi(x) \quad (4.4)$$

- Magnetic susceptibility:

$$\chi = V (\langle M^2 \rangle - \langle M \rangle^2) \quad (4.5)$$

- Modified magnetic susceptibility:

$$\chi' = V (\langle M^2 \rangle - \langle |M| \rangle^2) \quad (4.6)$$

- Binder cumulant [83]:

$$U_L = 1 - \frac{1}{3} \frac{\langle M^4 \rangle}{\langle M^2 \rangle^2}. \quad (4.7)$$

We introduced χ' so that in the broken-phase region one can effectively calculate the magnetic susceptibility for each sector separately [10, 26].

Our testing dataset is comprised of 1024 chains of configurations generated independently using HMC. Each HMC chain contains 100 configurations generated in sequence: the first 100 HMC iterations are for thermalization, followed by an additional 100 HMC iterations that we save. Each HMC iteration contains 20 leapfrog steps of step size 0.05. For estimating autocorrelations we use all of the testing dataset, while for computation of observables in Table 1 we only use the last configuration of each set, i.e., 1024 configurations.

We show values of the observables (4.4)-(4.7) computed across the diffusion and HMC ensembles in Table 1. We observe that, after reweighting, observables computed on the diffusion model data agree with both training and testing data.

Data Set	N_{conf}	$\langle M \rangle$	χ'	U_L
DM (Raw)	1024	0.5781(72)	3.38(15)	0.535(24)
DM (Reweighted)	1024	0.6289(72)	3.35(20)	0.559(26)
HMC (Testing)	1024	0.6143(74)	3.66(16)	0.547(22)
HMC (Training)	16384	0.6188(19)	3.63(4)	0.548(5)

Table 1: Mean values and standard errors for the observables defined in Eqs. (4.4), (4.6), and (4.7) computed on ensembles of $8 \times 8 \phi^4$ configurations. The comparison is between generated diffusion model (DM) data before and after reweighting with the HMC training and testing sets. The size of each dataset is labeled by the number of configurations N_{conf} .

The autocorrelation function for an observable \mathcal{O} is defined as

$$\Gamma_{\mathcal{O}}(t) := \langle \mathcal{O}_{t_0} \mathcal{O}_{t_0+t} \rangle - \langle \mathcal{O}_{t_0} \rangle \langle \mathcal{O}_{t_0+t} \rangle, \quad (4.8)$$

where t_0 is a source time and t is a time extent, or lag, along the Markov chain. We compare the normalized autocorrelation functions, $\bar{\Gamma}_{\mathcal{O}}(t) := \Gamma_{\mathcal{O}}(t)/\Gamma_{\mathcal{O}}(0)$, for a resampled diffusion-generated ensemble with HMC testing data in Fig. 8. We also compute the *integrated autocorrelation times* as in [92] for M on both datasets. The integrated autocorrelation time of a Markov chain of measurements of an observable \mathcal{O} is defined as

$$\tau_{\text{int}}(\mathcal{O}) := \frac{1}{2} + \lim_{t_{\text{max}} \rightarrow \infty} \sum_{t=1}^{t_{\text{max}}} \bar{\Gamma}_{\mathcal{O}}(t). \quad (4.9)$$

In Fig. 9, the HMC dataset is generated using 100 thermalization trajectories and an additional 20,000 HMC steps where every 20 samples are saved for computing the autocorrelation. Each HMC step consisted of 10 leapfrog steps at a step size of 0.1. Similarly, the diffusion dataset was generated by sampling from the trained model, using the Euler method with 200 ODE steps, and performing an accept/reject step on the proposed samples for a total of 1000 Monte Carlo iterations. We repeated the described procedure 100 times and illustrated the average in the figure. Using $t_{\text{max}} = 100$, we find

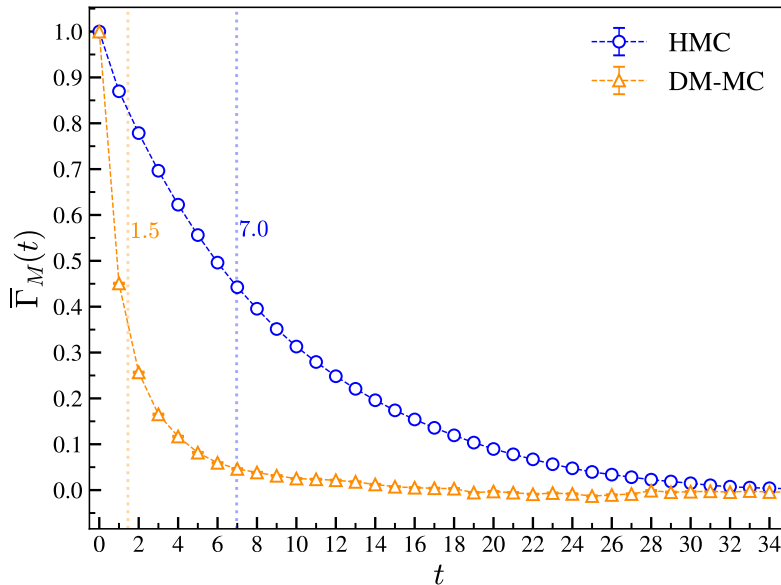


Figure 8: Normalized autocorrelation functions for the magnetization M , computed on 8×8 lattices from an HMC dataset and a resampled diffusion model dataset (DM-MC). The dotted lines represent the integrated autocorrelation times τ_{int} for each of the two ensembles.

$\tau_{\text{int}}^{\text{HMC}}(M) = 7.0$ and $\tau_{\text{int}}^{\text{DM-MC}}(M) = 1.5$ evaluated on the average of the autocorrelation over independent chains.

We note that while 200 leapfrog steps per configuration (10 leapfrog steps per trajectory, and 20 trajectories between saved configurations) are used for the HMC dataset, the diffusion model data in the comparison seen in Fig. 8 was generated with 200 ODE steps. This comparison indicates that the diffusion model significantly reduces autocorrelations along Markov Chains. We emphasize that these comparisons are valid only for this lattice size, and we leave a more detailed study of the volume scaling to future work.

An additional computational expense for the diffusion model arises from evaluating the U-Net, which is required for each iteration of the ODE solver. Nevertheless, we can freely choose more precise integrators to decrease the number of inference steps when sampling from a diffusion model. In contrast, HMC requires the introduction of auxiliary momenta and one must always use a symplectic integrator, such as the leapfrog method. Additionally, this analysis must be done in sequence for HMC, but the diffusion model can, in principle, generate all data in parallel.

4.3 Influence of Symmetry on Model Expressivity

A simple measure of model quality is to compare the true action $S[\phi]$ with the learned effective action $S_{\text{eff}}[\phi]$, each evaluated on the same batch of generated configurations. Qualitatively, these values should align well if the model is trained well, i.e. one should find $S_{\text{eff}}[\phi] \approx S[\phi] + c$, where c is an irrelevant normalization constant. Quantitatively, we can judge this alignment through the coefficient of determination R^2 between the two actions. In Fig. 9, we show the learned action in strong agreement with the true action

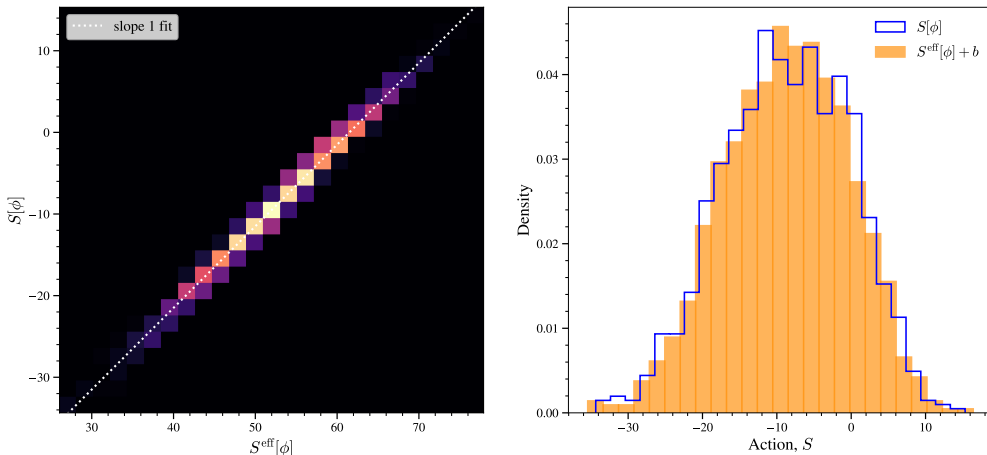


Figure 9: (Left) 2D histograms over 25 bins showing the distributions of the true action $S[\phi]$ against the effective action $S_{\text{eff}}[\phi]$ computed on an ensemble of $1024 \phi^4$ configurations sampled from a trained diffusion model near the critical point. The white dotted line represents a slope 1 fit with affine shift computed as the average difference between the actions: $b = \overline{S[\phi] - S_{\text{eff}}[\phi]}$. The correlation between the true and effective action is observed to be high; the corresponding R^2 coefficient is 0.9951. (Right) Histograms of the true action and effective action shifted by the fit constant b .

on an 8×8 lattice.

Perhaps a more illuminating measure of model quality is the effective sample size (ESS). As defined and discussed in Sect. 3.3, the ESS contains information about how importance weights are distributed across a generated ensemble. Moreover, the ESS is also correlated with the acceptance rate of a Metropolis accept/reject chain applied to the ensemble. The probability of accepting the next ‘proposal’ sample ϕ_i given the previous sample ϕ_{i-1} is given by

$$P_{\text{accept}}(\phi_i|\phi_{i-1}) = \min\left(1, \frac{p[\phi_i]/p[\phi_{i-1}]}{q[\phi_i]/q[\phi_{i-1}]}\right) = \min\left(1, \frac{w_i}{w_{i-1}}\right), \quad (4.10)$$

where the w_i are sample importance weights given by

$$w_i = \exp(-S[\phi_i] + S_{\text{eff}}[\phi_i]). \quad (4.11)$$

A low ESS indicates that the weights are heavily unbalanced, so the ratio of successive weights will often be small, leading to a low MCMC acceptance rate. Conversely, for a relatively higher ESS, the weights will be more stable and evenly spread, thus we expect higher acceptance rates when resampling our ensemble.

Notably, both the ESS and acceptance rate are highly sensitive to the reweighting factors w_i , whereas the R^2 coefficient is less sensitive to the overall spread in w . Moreover, these quantities display strikingly different scaling; we consistently obtain $R^2 > 0.95$ even when ESS and acceptance rates fall well below 10%. For this reason, we maintain that though the R^2 provides some heuristic insight into model performance, the ESS and acceptance rate are much more stringent benchmarks for the quality of generated samples.

Model Variant	ESS	R^2	Accept Rate
Standard U-Net ($\{e\}$)	0.11(1)	0.965(1)	0.25(1)
\mathbb{Z}_2 -Equiv. U-Net (\mathbb{Z}_2)	0.24(3)	0.980(1)	0.40(2)
Circular U-Net (\mathbb{T})	0.35(4)	0.987(1)	0.47(3)
$\mathbb{Z}_2 + \text{Circ.}$ U-Net ($\mathbb{Z}_2 \times \mathbb{T}$)	0.54(3)	0.992(1)	0.59(2)

Table 2: Effective sample sizes (ESS), R^2 coefficients, and MCMC resampling acceptance rates computed on 1024 diffusion-generated 8×8 ϕ^4 configurations in the broken phase, near the critical point for different U-Net variants trained for 250 epochs. The symbols in parentheses are shorthand notation for the symmetry group respected by the corresponding U-Net variant. Each experiment (training and sampling) was performed 10 times with the same parameters for each model architecture.

As discussed in Sec. 4.1, the ϕ^4 theory is \mathbb{Z}_2 -invariant, motivating the use of a \mathbb{Z}_2 -equivariant score network. Additionally, the periodicity of the lattice inspired us to use circular convolutional layers to respect the spacetime symmetry of the theory as well. Now we investigate the impact that these choices have on model performance and the quality of the samples produced therefrom.

There are four possible symmetry combinations: no symmetry, \mathbb{Z}_2 symmetry only, periodic translational symmetry (\mathbb{T}), as well as combined \mathbb{Z}_2 and \mathbb{T} symmetry. We compare the impacts of including each of these symmetry combinations on the ESS, R^2 , and acceptance rate for our trained models over ten repeated experiments performed with the same set of parameters during training and sampling. Consistently, we observe that including each symmetry yields significantly better performance across all three numerical metrics, with the highest level of performance being obtained when both symmetries are included. Including toroidal symmetry through circular convolutions has a much higher impact on improving model quality than including only \mathbb{Z}_2 equivariance. We summarize these results in Table 2 for the specific case of an Euler integrator with 500 inference steps. We consistently observe that the best performance is obtained with a network that is both antisymmetric in the field *and* spatially periodic.

Furthermore, our force regularization scheme, detailed in Eq. (2.19), provides a family of possible training regimes, parameterized continuously by the regularization coefficient c_0 . We observe that, when tuned properly, including the force regularization term dramatically improves model quality across all choices of symmetry when compared with models trained using traditional score matching ($c_0 \equiv 0$). In Table 3, we compare standard training and force-guided training with $c_0 = 0.1$.

Finally, we emphasize that generating these samples with an RK4 integrator was one choice out of many possible methods to solve the probability flow ODE. In practice, diffusion models enjoy a plethora of sampling methods for improving predictions and reducing discretization errors. For example, higher-order integrators may be used to solve the differential equations with better precision. Other sampling techniques involving predictor-corrector methods or adjustment techniques, such as the Metropolis-adjusted Langevin algorithm (MALA) [9], are also available.

For this study, we limited our scope to Euler and RK4 integrators for generating samples. The upper and lower panels of Table 3 display a comparison between model quality when using each of these ODE solvers. These effects must simultaneously take into account the computational cost that each integration technique incurs. We measure this

Sym.	No Regularization				Force Reg. ($c_0 = 0.1$)			
	NFE (\downarrow)	ESS (\uparrow)	R^2 (\uparrow)	Acc. (\uparrow)	NFE (\downarrow)	ESS (\uparrow)	R^2 (\uparrow)	Acc. (\uparrow)
<i>Euler Integrator ($N_{\text{step}} = 500$)</i>								
{ e }	500	0.107(12)	0.9650(08)	0.248(13)	500	0.250(26)	0.9840(05)	0.426(10)
\mathbb{Z}_2	1000	0.239(30)	0.9798(09)	0.398(15)	1000	0.432(26)	0.9902(05)	0.535(12)
\mathbb{T}	500	0.347(43)	0.9867(14)	0.469(28)	500	0.559(23)	0.9935(04)	0.594(15)
$\mathbb{Z}_2 \times \mathbb{T}$	1000	0.536(28)	0.9921(06)	0.594(18)	1000	0.707(13)	0.9958(02)	0.686(07)
<i>Runge-Kutta (RK4) Integrator ($N_{\text{step}} = 500$)</i>								
{ e }	2000	0.129(16)	0.9619(25)	0.280(19)	2000	0.274(25)	0.9834(04)	0.445(12)
\mathbb{Z}_2	4000	0.220(30)	0.9807(08)	0.419(28)	4000	0.507(27)	0.9913(03)	0.562(11)
\mathbb{T}	2000	0.359(28)	0.9859(11)	0.482(10)	2000	0.579(20)	0.9938(04)	0.611(07)
$\mathbb{Z}_2 \times \mathbb{T}$	4000	0.562(30)	0.9926(06)	0.612(35)	4000	0.707(24)	0.9959(02)	0.684(13)

Table 3: Comparison of ESS, R^2 , and MCMC acceptance rates for U-Net symmetry variants evaluated on 1024 diffusion-generated configurations (repeated 10 times for error estimation). Rows are grouped by ODE integrator (*Euler* and *RK4*), while columns compare standard training (No Reg.) versus force-regularized training ($c_0 = 0.1$). The NFE subcolumn denotes the total number of score function evaluations during the ODE solve. The symbols in the Sym. column correspond to the same group symmetries as those in Table 2. The arrows ($\uparrow\downarrow$) indicate whether the corresponding quantity is preferred to take higher or lower values.

cost with the number of function evaluations (NFE), which counts how many times the score network must be evaluated during each integration step and multiplies this count by the total number of ODE solver iterations. The baseline is 1 evaluation for Euler and 4 evaluations for RK4 (per integration step), but these are doubled for the \mathbb{Z}_2 -equivariant network due to the antisymmetrization. On average, we observe little appreciable improvement in the three model quality metrics when using the RK4 integrator over the Euler integrator.

5 Application to U(1) Gauge Theory in 2D

We use the angular representation of U(1) gauge theory in two spacetime dimensions and define the U(1) lattice action as

$$S[\theta] = -\beta \sum_x \sum_{\mu < \nu} \cos \phi_{\mu\nu}(x), \quad (5.1)$$

where the angular plaquettes depend on the link phases $\theta_\mu(x)$

$$\phi_{\mu\nu}(x) = \theta_\mu(x) + \theta_\nu(x + \hat{\mu}) - \theta_\mu(x + \hat{\nu}) - \theta_\nu(x), \quad (5.2)$$

and $\phi_{\mu\nu}$ form gauge-invariant objects on the lattice (c.f. Fig. 10). For further details on the formulation of U(1) gauge theory on the lattice, we direct the reader to Appendix A.1.

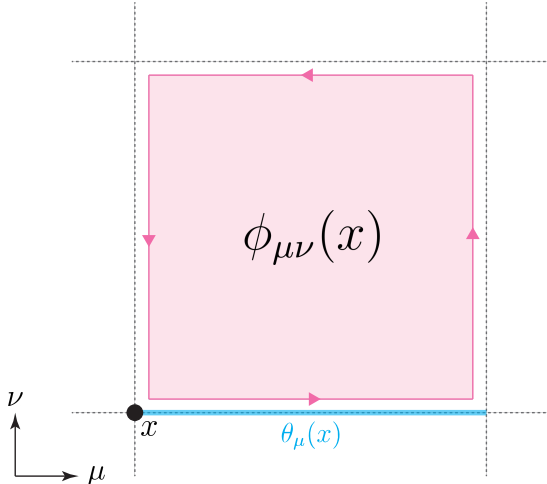


Figure 10: A plaquette phase in the (μ, ν) plane based at a lattice site x . The angular link variable $\theta_\mu(x)$ between sites x and $x + \hat{\mu}$ is highlighted in cyan. The group-valued plaquette and the angular plaquette are related via the exponential map: $P_{\mu\nu}(x) = e^{i\phi_{\mu\nu}(x)}$.

5.1 Gauge-Equivariant Score Network

The force for the U(1) gauge theory on the lattice is given by

$$\mathbf{s}(\theta_\mu(x)) = \beta \sum_{\nu} [\sin \phi_{\mu\nu}(x) - \sin \phi_{\mu\nu}(x - \hat{\nu})], \quad (5.3)$$

which corresponds to the true score function with respect to the algebra-valued $\theta_\mu(x)$. For a derivation of Eq. (5.3), see Appendix A.2. The most notable property of the force in Eq. (5.3) is that it is *gauge-invariant*, as it only depends on plaquette phases $\phi_{\mu\nu}$. We therefore aim to construct a score network that respects gauge symmetry.

To build an explicitly gauge-invariant score network, we make our network a function of gauge-invariant quantities. On their own, the gauge links angles $\theta_0(x), \theta_1(x)$ are gauge-variant, but can be composed into plaquette phases $\phi_{01}(x)$, thereby giving a set of gauge-invariant data. Then, any transformation that the score network applies will remain agnostic to gauge-transformations on the links. In contrast to other approaches like data augmentation where one applies random gauge transformations to the input training data, our approach exactly enforces U(1) gauge symmetry.

To parameterize our score network, we again use a U-Net with circularly-padded convolutional layers to respect the lattice’s periodic boundaries, as described in Sec. 4.1. The gauge-invariant U-Net is constructed such that it takes in data with a single channel (the plaquette phases), and returns data with two channels ($N_d = 2$ spacetime directions) to represent a score function with respect to gauge links.

We train on 65,536 U(1) configurations generated with 1000 HMC iterations (following 200 thermalization steps) of step size 0.1 and 10 leapfrog steps per trajectory. All models were trained for 500 epochs with learning rate 5×10^{-4} and batch size 512. The testing dataset to which we compare consists of 8192 configurations generated via the same method.

After training, we visualize the inference process by tracking certain quantities over reverse diffusion time. An important quantity for tracking the exploration of phase space is the *topological charge* [86]. In two dimensions, the U(1) theory topological charge is

defined by

$$Q := \frac{1}{2\pi} \sum_x \phi_{01}(x), \quad (5.4)$$

and is integer-valued. Intuitively, Q counts how many times the gauge fields ‘wrap around’ the group $U(1)$ along closed spacetime loops. In this case, the plaquette phase is measured at each lattice site to measure how much circulation the gauge field has. The global flux can be studied by examining this phase across the entire lattice, and the overall winding number labels different topological sectors of the theory. In Fig. 11 we plot the evolution of the average plaquette and topological charge during the reverse process. While we see variations of the topological charge over a broad range during the diffusion-based sampling, the effect of autocorrelations of the topological charge on the observables of interest is yet to be explored.

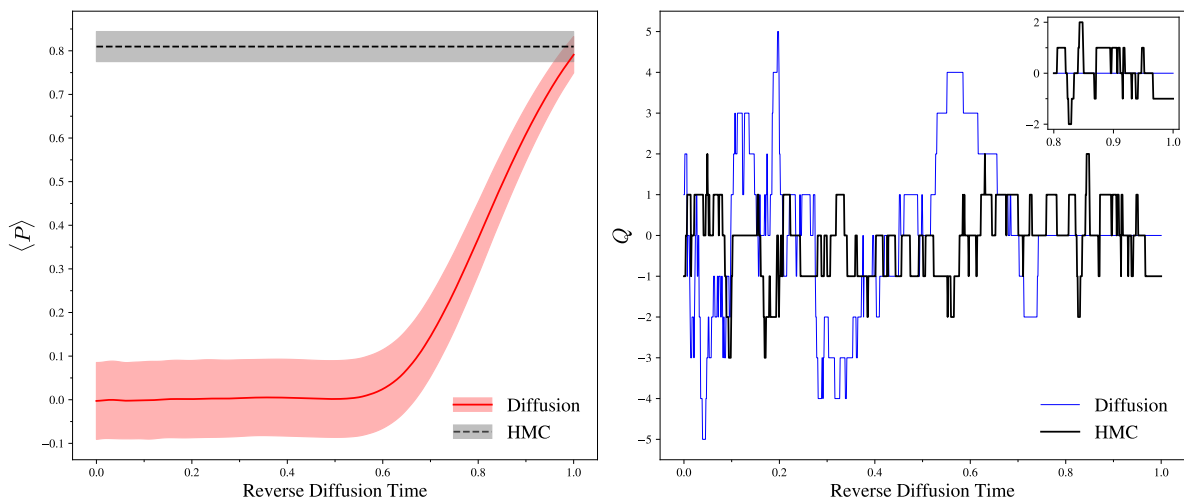


Figure 11: Progression over reverse diffusion time of the (left) average plaquette $\langle P \rangle$ with 1σ error bands over the lattice and the (right) topological charge Q of a randomly chosen configuration each from the diffusion-generated and HMC ensembles of 8×8 lattices at $\beta = 3.0$. As expected, the value of the average plaquette is seen to gradually rise to match that of the HMC test ensemble.

5.2 Additional Observables

In the $U(1)$ theory, we compute expectation values of rectangular $R \times T$ Wilson loops, where R and T are spatial and temporal extents across the lattice, respectively. In Figure 12, we compare Wilson loops between the HMC and diffusion-generated data with the exact results on a 8×8 lattice at $\beta = 3.0$ and see good agreement. Exact results are obtained using the weighting factors $w_i = \frac{p_i}{q_i}$ to compute reweighted means and errors of the observables of interest, as outlined in Sec. 2.4. We also compute *topological susceptibility*, formally defined as

$$\chi_Q := \frac{\langle Q^2 \rangle}{V}. \quad (5.5)$$

The topological susceptibility is associated with the fluctuations of the topological charge, and while its computation in lattice QCD poses many challenges [72, 73, 74, 75, 76], the simple angular definition of Q in Eq. (5.4) allows a straightforward computation of χ_Q in

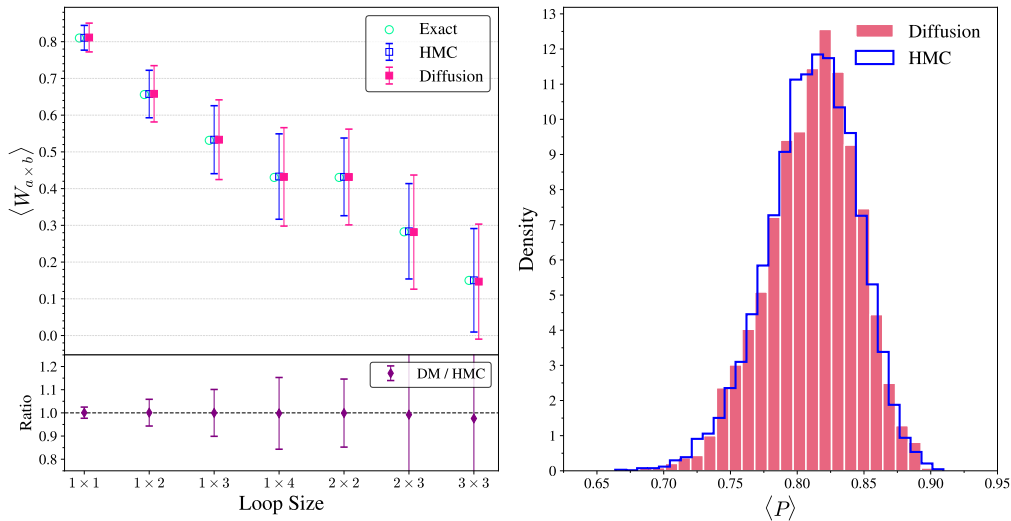


Figure 12: (Left) rectangular Wilson loops of different sizes $a \times b$, computed on 8192 configurations each from a trained diffusion model and an HMC test dataset for Abelian gauge theory at $\beta = 3.0$ on an 8×8 lattice. We also plot the exact values against the numerical estimates. (Right) normalized histograms of reweighted average plaquette values from the diffusion model and HMC test set.

U(1) lattice gauge theory. Table 4 lists reweighted measurements of $\langle P \rangle$ and χ_Q , which show good agreement between the data obtained with HMC and the diffusion model.

β	Ensemble	$\langle P \rangle$	χ_Q
1.0	HMC	0.4465(8)	0.0406(6)
	Diffusion	0.4472(8)	0.0404(6)
2.0	HMC	0.6977(6)	0.0193(3)
	Diffusion	0.6971(6)	0.0195(3)
3.0	HMC	0.8099(4)	0.0109(2)
	Diffusion	0.8094(4)	0.0104(2)

Table 4: Comparison of observables for 8×8 lattices and couplings $\beta \in \{1, 2, 3\}$ between diffusion-generated and HMC ensembles. The HMC ensemble contains 8192 independent configurations, each generated with 200 thermalization trajectories. The diffusion ensemble also contains 8192 configurations, and its observables are reweighted.

We obtain effective sample sizes in the range of 15% to 65% for the ensembles in Table 4. The likelihood computation becomes more challenging with increasing lattice size; the ESS decreases with increasing volume, thereby reducing the efficiency of using the diffusion model to produce precise estimates for observables. As an alternative method, Ref. [77] applies the Metropolis-adjusted Langevin algorithm (MALA) during the sampling phase for U(1) gauge theory. We reserve these ongoing investigations for future work.

6 Conclusions and Outlook

In this work, we develop symmetry-preserving diffusion models and subsequently test them on two-dimensional ϕ^4 field theory and U(1) gauge theory. Through several numerical experiments, we demonstrate that our symmetry-preserving diffusion models produce ensembles yielding accurate physical observables. We show that our score networks correctly approximate the force fields and correctly learn to sample from the target densities, which is enhanced by enforcing symmetry. We employ a modified version of score matching that improved the quality of our models. It is noteworthy that score matching is a fast training procedure, which is particularly efficient in comparison to training continuous flow-based models that require the additional step of forward passes through ODE solvers. We validate the proposed diffusion models by comparing several key observables with conventional sampling approaches.

We quantify our model’s performance by computing effective sample sizes (ESS) and acceptance rates for resampled ensembles, where we find that our generated ensembles display significantly less autocorrelation after resampling compared to HMC data. As discussed, although this improvement comes at the cost of increased computational expense, it can be trivially parallelized. Most encouragingly, we illustrate that our paradigm, which combines force-regularization in training and encoding explicit symmetries, yields models that achieve much stronger performance than non-equivariant baselines. While this is a promising start, to establish scalability, it is still necessary to examine the performance of this framework in higher dimensions and with much larger lattice sizes.

Diffusion models are naturally amenable to different different methods of sampling, several of which are detailed in Ref. [45]. Langevin dynamics has been applied to solve the reverse SDE [47, 48] with different implementations. Other modifications include SDE solvers with adaptive step sizes [49] and explicit predictor-corrector methods [44]. While we do not consider these additional sampling methods in this study, they form interesting and necessary avenues to explore in future work. Examining how different integrators, predictor-correctors, and other methods can impact the quality of generated samples is an important direction for future research on this topic.

Another natural future direction is to extend our framework to non-abelian gauge theories, especially SU(3), towards simulating QCD. The primary aim would be to design score networks that exactly respect SU(N) symmetries. Integrating fermions into these models should be straightforward [77] because pre-generated gauge configurations will already include all information about fermionic determinants. Nevertheless, the score function may need to be more expressive due to the non-locality of the fermion determinant. It would also be interesting to scrutinize the ϕ^4 theory more deeply in this context. In particular, diffusion models could be used to characterize the phase transitions and criticality of the theory. This also creates a strong opportunity for testing more advanced score network architectures. Additionally, developing a better understanding of how hyperparameters—both at the training and inference stages— influence sample quality would be extremely useful for scaling models upwards.

To echo the conclusions of Ref. [23], we emphasize that diffusion models, like normalizing flows, each represent just one approach in a much broader taxonomy of next-generation deep generative models and ML-enhanced sampling techniques for LQFT. Developing a fuller perspective on the future capabilities of the methods proposed here will depend not on anticipating the ever-changing landscapes of the LQFT and ML research fields, but rather on adapting to oncoming advancements, likely resulting in a

hybrid strategy involving conventional and ML-based methods.

Acknowledgments

The authors are thankful to Gert Aarts and Lingxiao Wang for correspondence and helpful comments, and Antoine Misery for his work in the early stages of the project. OV and AXK acknowledge the ETH Zürich Institute for Theoretical Physics and the Pauli Center for Theoretical Studies for support and hospitality in summers 2024 and 2025, as well as the Mainz Institute for Theoretical Physics (MITP) of the Cluster of Excellence PRISMA⁺ (Project ID 390831469) for its hospitality and support. AXK and MKM thank the Kavli Institute for Theoretical Physics (KITP) for hospitality and support during the program “What is Particle Theory?” The KITP is supported in part by the National Science Foundation under Grant No. PHY-2309135. MKM is grateful for the hospitality of Perimeter Institute where part of this work was carried out. Research at Perimeter Institute is supported in part by the Government of Canada through the Department of Innovation, Science and Economic Development and by the Province of Ontario through the Ministry of Colleges and Universities. This research was also supported in part by the Simons Foundation through the Simons Foundation Emmy Noether Fellows Program at Perimeter Institute. AXK and OV acknowledge support from the U.S. Department of Energy, Office of Science under grant Contract Number DE-SC0015655. JK and MKM acknowledge the support received from the Horizon Europe project interTwin, funded by the European Union Grant Agreement Number 101058386. OV acknowledges support from a University of Illinois Graduate College Fellowship, as well as from a Sloan Scholarship through the Alfred P. Sloan Foundation’s University Center of Exemplary Mentoring, awarded in 2023-2024. Numerical experiments and data analysis were carried out with PyTorch [93], NumPy [94], and SciPy [95]. Figures were produced using the `matplotlib` library [96] as well as Adobe Illustrator [97]. Almost all computational work in this project was performed on a single NVIDIA TITAN Xp GPU through the ETH D-PHYS `spacem14` compute node. Some of the experiments in this research used the DeltaAI advanced computing and data resource, which is supported by the National Science Foundation (award OAC 2320345) and the State of Illinois. DeltaAI is a joint effort of the University of Illinois Urbana-Champaign and its National Center for Supercomputing Applications. Access to DeltaAI was provided in part by the Illinois Computes project which is supported by the University of Illinois Urbana-Champaign.

A Lattice Field Theory Formalism

Here we present further details on the formulation of relevant aspects of LQFT which supplement the intuitions presented in the main body of our work.

A.1 Pure U(1) Lattice Gauge Theory

A U(1) gauge theory in continuous Minkowski spacetime can be defined by the Maxwell Lagrangian density:

$$\mathcal{L} = -\frac{1}{4}F_{\mu\nu}F^{\mu\nu}, \quad (\text{A.1})$$

where the components of the abelian field strength tensor $F_{\mu\nu}$ are given by

$$F_{\mu\nu} = \partial_\mu A_\nu - \partial_\nu A_\mu. \quad (\text{A.2})$$

This Lagrangian is invariant under local U(1) transformations, represented as translations of the gauge field by a gradient:

$$A_\mu(x) \mapsto A_\mu(x) + \partial_\mu \alpha(x) \quad (\text{A.3})$$

where α is an arbitrary scalar-valued function. In the defining, one-dimensional representation of the Lie group U(1), the gauge degrees of freedom $A_\mu \in \mathfrak{u}(1)$ are algebra-valued spacetime vector fields which play the role of affine connections for the gauge group. When discretizing the pure U(1) theory onto the lattice, one replaces the algebra-valued gauge fields A_μ with group-valued parallel transporters U_μ , called *gauge links*, defined as path-ordered Wilson lines between infinitesimally separated adjacent lattice sites:

$$U_\mu(x) := \mathcal{P} \exp \left\{ i \int_x^{x+\hat{\mu}} A_\nu(y) dy^\nu \right\}. \quad (\text{A.4})$$

For sufficiently smoothly varying gauge fields, the limit of small lattice spacing allows us to replace A_μ by an approximately constant phase parameter $\theta_\mu \in [-\pi, \pi)$. Then the gauge links can simply be written as complex phases $U \in \mathbb{C}$:

$$U_\mu(x) = e^{i\theta_\mu(x)}. \quad (\text{A.5})$$

Under arbitrary gauge transformations $\Omega(x) \in \text{U}(1)$, the links transform via

$$U_\mu(x) \mapsto \Omega(x)U_\mu(x)\Omega^*(x + \hat{\mu}). \quad (\text{A.6})$$

Gauge-invariant quantities on the lattice are therefore constructed as products of link variables around closed loops, since any closed loop that starts and ends at a lattice site x will transform via conjugation by $\Omega(x)$. Since U(1) is abelian, gauge-invariance is trivial as the conjugation leaves the loop unchanged. As such, the gauge-invariant U(1) lattice action is written as

$$S[U] = -\beta \sum_x \sum_{\mu < \nu} \Re P_{\mu\nu}(x), \quad (\text{A.7})$$

where β corresponds to an inverse coupling strength and $P_{\mu\nu}$ are the smallest gauge-invariant units that can be constructed on the lattice, called *plaquettes*, defined as

$$P_{\mu\nu}(x) := U_\mu(x)U_\nu(x + \hat{\mu})U_\mu^*(x + \hat{\nu})U_\nu^*(x). \quad (\text{A.8})$$

Since both U(1) gauge links and gauge transformations are elements of a one-parameter compact Lie group, we may adopt the one-dimensional *angular representation* in which we parameterize the transformations as complex phases as well:

$$\Omega(x) = e^{i\omega(x)} \quad (\text{A.9})$$

such that the gauge transformation of a link variable can be fully specified in the Lie algebra as

$$\theta_\mu(x) \mapsto \omega(x) + \theta_\mu(x) - \omega(x + \hat{\mu}). \quad (\text{A.10})$$

Furthermore, plaquettes can be written more simply in the angular representation as

$$\phi_{\mu\nu}(x) := \theta_\mu(x) + \theta_\nu(x + \hat{\mu}) - \theta_\mu(x + \hat{\nu}) - \theta_\nu(x), \quad (\text{A.11})$$

where we make the identification that $P_{\mu\nu} = e^{i\phi_{\mu\nu}}$. Furthermore, one can easily show that $\phi_{\mu\nu}(x)$ is invariant under transformations of the form (A.10), so gauge-invariance is preserved in the angular representation. Having parameterized both gauge links θ and gauge transformations Ω as real-valued phases in the compact algebra $\omega \in [-\pi, \pi] \cong \mathfrak{u}(1)$, we may write down the U(1) lattice action:

$$S[\theta] = -\beta \sum_x \sum_{\mu < \nu} \cos \phi_{\mu\nu}(x), \quad (\text{A.12})$$

where one immediately sees that this action must be gauge-invariant since it is written entirely in terms of gauge-invariant plaquette phases.

A.2 Derivation of the U(1) Force

In this section we present an analytical derivation of the exact U(1) force. For further reading and comparison of results, we direct readers to section 8.3 of Ref. [79], where the SU(3) force is similarly computed for use in the HMC algorithm.

In the numerical experiments presented in Sec. 5, the relevant data are the link angles $\theta_\mu(x)$ corresponding to the gauge field configurations. As explicated in Appendix A.1, the U(1) gauge action in the angular representation takes the form

$$S[\theta] = -\beta \sum_{x \in \mathbb{L}} \sum_{\mu=1}^{N_d} \sum_{\nu=\mu+1}^{N_d} \cos \phi_{\mu\nu}(x). \quad (\text{A.13})$$

To compute the score function, we must differentiate with respect to a fixed angle configuration in some direction $\alpha \in \{1, \dots, N_d\}$ at some lattice site $y \in \mathbb{L}$. Using the chain rule, we have:

$$\mathbf{s}(\theta_\alpha(y)) = -\frac{\partial}{\partial \theta_\alpha(y)} S[\theta] \quad (\text{A.14})$$

$$= -\beta \sum_{x \in \mathbb{L}} \sum_{\mu=1}^{N_d} \sum_{\nu=\mu+1}^{N_d} \sin \phi_{\mu\nu}(x) \frac{\partial \phi_{\mu\nu}(x)}{\partial \theta_\alpha(y)} \quad (\text{A.15})$$

Then differentiating the plaquette angle will yield

$$\frac{\partial \phi_{\mu\nu}(x)}{\partial \theta_\alpha(y)} = \delta_{x,y} \delta_{\mu\alpha} + \delta_{x+\hat{\mu},y} \delta_{\nu\alpha} - \delta_{x+\hat{\nu},y} \delta_{\mu\alpha} - \delta_{x,y} \delta_{\nu\alpha} \quad (\text{A.16})$$

$$= \delta_{\mu\alpha} (\delta_{x,y} - \delta_{x+\hat{\nu},y}) + \delta_{\nu\alpha} (\delta_{x+\hat{\mu},y} - \delta_{x,y}). \quad (\text{A.17})$$

Before moving on, we note a few properties of the plaquette angle for all lattice sites $x \in \mathbb{L}$:

- If the directions are the same, the angle vanishes:

$$\phi_{\mu\mu}(x) = 0$$

- Under the transposition $\mu \leftrightarrow \nu$, the plaquette is negated:

$$\phi_{\mu\nu}(x) = -\phi_{\nu\mu}(x)$$

Using these facts, the double sum over spacetime directions that appears in the action may be rewritten in a more symmetric fashion:

$$\sum_{\mu=1}^{N_d} \sum_{\nu=\mu+1}^{N_d} \rightarrow \frac{1}{2} \sum_{\mu=1}^{N_d} \sum_{\nu=1}^{N_d}. \quad (\text{A.18})$$

Continuing our computation of the score function, we now have

$$\begin{aligned} \mathbf{s}(\theta_\alpha(y)) &= -\frac{\beta}{2} \sum_{x \in \mathbb{L}} \sum_{\nu=1}^{N_d} (\delta_{x,y} - \delta_{x+\hat{\nu},y}) \sin \phi_{\alpha\nu}(x) \\ &\quad - \frac{\beta}{2} \sum_{x \in \mathbb{L}} \sum_{\mu=1}^{N_d} (\delta_{x+\hat{\mu},y} - \delta_{x,y}) \sin \phi_{\mu\alpha}(x), \end{aligned} \quad (\text{A.19})$$

where we used the Kronecker deltas to complete the inner sums over μ and ν in the first and second terms, respectively. Summing over the lattice sites gives

$$\begin{aligned} \mathbf{s}(\theta_\alpha(y)) &= -\frac{\beta}{2} \sum_{\nu} (\sin \phi_{\alpha\nu}(y) - \sin \phi_{\alpha\nu}(y - \hat{\nu})) \\ &\quad - \frac{\beta}{2} \sum_{\mu} (\sin \phi_{\mu\alpha}(y - \hat{\mu}) - \sin \phi_{\mu\alpha}(y)). \end{aligned} \quad (\text{A.20})$$

Relabeling the summed indices μ and ν to another index γ and using the antisymmetry of the angle plaquette gives the final result:

$$\mathbf{s}(\theta_\alpha(y)) = -\beta \sum_{\gamma=1}^{N_d} [\sin \phi_{\gamma\alpha}(y) - \sin \phi_{\gamma\alpha}(y - \hat{\gamma})]. \quad (\text{A.21})$$

By inspection, it becomes immediately clear that $\mathbf{s}(\theta)$ is U(1)-invariant in the angular representation, since it is built entirely out of gauge-invariant plaquette phases $\phi_{\mu\nu}$.

B Stochastic Dynamics of Scalar Fields

B.1 Derivation of the Fokker-Planck Equation

In this section, we derive the Fokker-Planck (FP) equation for scalar fields following Ref. [84]. This equation describes the time evolution of the probability density function (PDF) $p_t(\phi_t)$. We denote a scalar field by $\phi_t(x)$, where x corresponds to a lattice site and $t \geq 0$ indexes the fictitious diffusion time. For brevity, we will suppress the position

dependence and use the shorthand ϕ_t . The forward diffusion process can be expressed as the SDE:

$$\frac{d\phi_t}{dt} = f(\phi_t) + \sigma\eta_t, \quad (\text{B.1})$$

where $f(\phi_t)$ represents a deterministic drift term, η_t is a stochastic term that we set to the standard white Gaussian noise, and σ is constant with respect to the scalar field, but it can depend on time. For a small step size h in time, we have

$$\phi_{t+h} = \phi_t + hf(\phi_t) + \sqrt{h}\sigma \int_t^{t+h} \frac{d\tau}{\sqrt{h}} \eta_\tau, \quad (\text{B.2})$$

where we neglected all terms of size $\mathcal{O}(h^{3/2})$ or higher. The integral yields another noise term with zero mean and unit variance. First, we calculate the conditional PDF of $\phi_{t+h} = \varphi$ at time $t+h$ subject to $\phi_t = \varphi_0$ at time t :

$$\begin{aligned} p_{t+h|t}(\varphi|\varphi_0) &= \mathbb{E}_\eta \left[\delta \left(\varphi - \varphi_0 - hf(\varphi_0) - \sqrt{h}\sigma\eta \right) \right] \\ &= \int \frac{d\zeta}{(2\pi)^n} e^{i\zeta \cdot (\varphi - \varphi_0 - hf(\varphi_0))} \mathbb{E}_\eta \left[e^{-i\zeta \cdot \sqrt{h}\sigma\eta} \right] \\ &= \int \frac{d\zeta}{(2\pi)^n} e^{i\zeta \cdot (\varphi - \varphi_0 - hf(\varphi_0))} e^{-\frac{h\sigma^2}{2}\zeta \cdot \zeta}. \end{aligned} \quad (\text{B.3})$$

Here, we treat φ as a vector of dimension n , and the delta function is understood as a product of n delta functions over the components of the vector. In the second line, we used the Fourier representation of the delta function by introducing ζ as a vector of the same size of φ . Then, $p_{t+h}(\varphi)$ can be expressed as

$$\begin{aligned} p_{t+h}(\varphi) &= \int d\varphi_0 p_{t+h|t}(\varphi|\varphi_0) p_t(\varphi_0) \\ &= \int d\varphi_0 \int \frac{d\zeta}{(2\pi)^n} e^{i\zeta \cdot (\varphi - \varphi_0 - hf(\varphi_0))} e^{-\frac{h\sigma^2}{2}\zeta \cdot \zeta} p_t(\varphi_0). \end{aligned} \quad (\text{B.4})$$

The time derivative of $p_t(\phi_t)$ then reads

$$\begin{aligned} \frac{\partial}{\partial t} p_t(\varphi) &= \lim_{h \rightarrow 0} \frac{p_{t+h}(\varphi) - p_t(\varphi)}{h} \\ &= \int d\varphi_0 \lim_{h \rightarrow 0} \frac{p_{t+h|t}(\varphi|\varphi_0) - p_{t|t}(\varphi|\varphi_0)}{h} p_t(\varphi_0) \\ &= \int d\varphi_0 \int \frac{d\zeta}{(2\pi)^n} e^{i\zeta \cdot \varphi} e^{-i\zeta \cdot \varphi_0} \left(-i\zeta \cdot f(\varphi_0) - \frac{\sigma^2}{2} \zeta \cdot \zeta \right) p_t(\varphi_0) \\ &= \int d\varphi_0 \delta(\varphi - \varphi_0) \left(-\nabla \cdot f(\varphi_0) + \frac{\sigma^2}{2} \nabla \cdot \nabla \right) p_t(\varphi_0) \\ &= \nabla \cdot \left(-f(\varphi) + \frac{\sigma^2}{2} \nabla \right) p_t(\varphi). \end{aligned} \quad (\text{B.5})$$

In deriving the fourth line, we applied integration by parts and assumed that the integrand vanishes at the boundaries. This concludes our derivation of the Fokker-Planck equation.

B.2 Reverse Langevin Process

We now discuss the reverse process in Langevin dynamics. To this end, we introduce a function g and a SDE as

$$\frac{d\phi_t}{dt} = g(\phi_t) + \tilde{\sigma}\eta_t, \quad (\text{B.6})$$

where η_t is the standard white Gaussian noise and $\tilde{\sigma}$ is constant with respect to the scalar field, but it can depend on time. We demand equation (B.6) to be the reverse of equation (B.1) in the following sense: a sequential evolution of the random field ϕ_{t_1} governed by equation (B.1) from time t_1 to t_2 and by equation (B.6) from t_2 to t_1 must not change the PDF of the random field. In other words, the FP equations of the forward and reverse processes must be the same. We show below that the condition holds if we set

$$g(\phi_t) = f(\phi_t) - \frac{\sigma^2 + \tilde{\sigma}^2}{2} \nabla \log p_t(\phi_t). \quad (\text{B.7})$$

We now present the proof. We use $p_t(\phi_t)$ and $q_t(\phi_t)$ to denote the PDF of ϕ_t in the forward and reverse processes, respectively. The aim is to obtain the function g such that $q_t(\phi_t) = p_t(\phi_t)$. Having already derived the FP equation for $p_t(\phi_t)$, we now derive the corresponding equation for $q_t(\phi_t)$. For a small h , equation (B.6) can be solved backward in time as

$$\phi_{t-h} = \phi_t - hg(\phi_t) + \sqrt{h}\tilde{\sigma} \int_t^{t-h} \frac{d\tau}{\sqrt{h}} \eta_\tau, \quad (\text{B.8})$$

where we neglected all terms of size $h^{3/2}$ or smaller. Similar to the forward process, the integral yields another normal noise with zero mean and unit variance independent of the overall sign. The conditional PDF of $\phi_{t-h} = \varphi$ at time $t-h$ subject to $\phi_t = \varphi_0$ at time t reads

$$\begin{aligned} q_{t-h|t}(\varphi|\varphi_0) &= \mathbb{E}_\eta \left[\delta \left(\varphi - \varphi_0 + hg(\varphi_0) + \sqrt{h}\tilde{\sigma}\eta \right) \right] \\ &= \int \frac{d\zeta}{(2\pi)^n} e^{i\zeta \cdot (\varphi - \varphi_0 + hg(\varphi_0))} e^{-\frac{h\tilde{\sigma}^2}{2} \zeta \cdot \zeta}. \end{aligned} \quad (\text{B.9})$$

Note that there is a mismatch between the sign of the terms with h in equations (B.3) and (B.9). Because of the mismatch, the FP equation of the reverse process looks different:

$$\begin{aligned} \frac{\partial}{\partial t} q_t(\varphi) &= \lim_{h \rightarrow 0} \frac{q_{t-h}(\varphi) - q_t(\varphi)}{-h} \\ &= \nabla \cdot \left(-g(\varphi) - \frac{\tilde{\sigma}^2}{2} \nabla \right) q_t(\varphi). \end{aligned} \quad (\text{B.10})$$

Defining g as in equation (B.7) removes the apparent difference and makes both FP equations identical (we assume there is a fixed time at which p and q are equal).

It is noteworthy that this is a *family* of reverse processes for the diffusion process, parameterized by $\tilde{\sigma}$ that can also be time-dependent. Remarkably, when $\tilde{\sigma}$ vanishes, the reverse process reduces to a deterministic differential equation.

B.3 Solving the FP Equation along ODE Trajectories

In this section, we provide a solution to the FP equation and relate it to the probability flow ODE for samples in reverse diffusion time. We suppose that samples ϕ_t evolve in reverse time according to the deterministic process where $\tilde{\sigma} = 0$ in Eq. (B.6):

$$\frac{d\phi_t}{dt} = f(\phi_t, t) - \frac{\sigma^2}{2} \nabla \log p_t(\phi_t). \quad (\text{B.11})$$

The total time derivative of the log density is then, by the chain rule:

$$\frac{d}{dt} \log p_t(\phi_t) = \frac{\partial}{\partial t} \log p_t(\phi_t) + \frac{d\phi_t}{dt} \cdot \nabla \log p_t(\phi_t). \quad (\text{B.12})$$

The FP equation for p_t is

$$\partial_t p_t = -\nabla \cdot (f p_t) + \frac{\sigma^2}{2} \nabla^2 p_t, \quad (\text{B.13})$$

which yields

$$\frac{\partial}{\partial t} \log p_t = \frac{1}{p_t} \left(-p_t \nabla \cdot f - f \cdot \nabla p_t + \frac{\sigma^2}{2} \nabla^2 p_t \right). \quad (\text{B.14})$$

Substituting into (B.12), we get

$$\frac{d}{dt} \log p_t = -\nabla \cdot f - f \cdot \nabla \log p_t + \frac{\sigma^2}{2} \frac{\nabla^2 p_t}{p_t} + \frac{d\phi_t}{dt} \cdot \nabla \log p_t.$$

Substituting the deterministic flow for ϕ_t and replacing $\nabla \log p_t(\cdot)$ with $\mathbf{s}(\cdot, t)$, we have

$$\frac{d}{dt} \log p_t(\phi_t) = -\nabla \cdot f - f \cdot \mathbf{s} + \frac{\sigma^2}{2} (\|\mathbf{s}\|^2 + \nabla \cdot \mathbf{s}) + \left(f - \frac{\sigma^2}{2} \mathbf{s} \right) \cdot \mathbf{s} \quad (\text{B.15})$$

$$= -\nabla \cdot f(\phi_t, t) + \frac{\sigma^2}{2} \nabla \cdot \mathbf{s}(\phi_t, t). \quad (\text{B.16})$$

Hence, the total derivative along the probability flow ODE trajectory is simply

$$\frac{d}{dt} \log p_t(\phi_t) = -\nabla \cdot \left(f(\phi_t, t) - \frac{\sigma^2}{2} \mathbf{s}(\phi_t, t) \right), \quad (\text{B.17})$$

whose solution is obtained as

$$p_t(\phi_t) = \exp \left[- \int_{t'}^t \nabla \cdot \left(f(\phi_\tau, \tau) - \frac{\sigma^2}{2} \mathbf{s}(\phi_\tau, \tau) \right) d\tau \right] p_{t'}(\phi_{t'}). \quad (\text{B.18})$$

The probability flow ODE gives a deterministic trajectory for samples ϕ_t that pushes probability mass, generating a *flow* of particles that matches the evolution of the density p_t . The pushforward of the starting distribution, p_0 , along these trajectories yields the same marginal densities as the solution to the FP equation.

C Construction of Equivariant Score Networks

C.1 Group Symmetries of Score Functions

Here, we examine the relationship between the symmetries of probability distributions and the resulting symmetries of their corresponding score functions. Some notation: We denote groups by \mathcal{G} and their algebras, when they exist, by \mathfrak{g} . Group elements are denoted $G \in \mathcal{G}$, and their representations by ρ_G . We use \mathcal{F} to abstractly denote field space, i.e. the space where field configurations live.

Definition C.1 (Invariance). Let \mathcal{G} be a group and let $f : \mathcal{X} \rightarrow \mathcal{X}$ be a function. Suppose an element $G \in \mathcal{G}$ acts on $x \in \mathcal{X}$ via $x \mapsto \rho_G(x)$, where ρ_G is the representation of G . We say that f is *invariant* to G , or G -invariant, if

$$(f \circ \rho_G)(x) = f(x) \quad (\text{C.1})$$

for every x . If Eq. (C.1) holds for all $G \in \mathcal{G}$, then we say f is invariant to \mathcal{G} , or \mathcal{G} -invariant.

Definition C.2 (Equivariance). Let \mathcal{G} be a group and $f : \mathcal{X} \rightarrow \mathcal{Y}$ be a function. We say f is *equivariant* to $G \in \mathcal{G}$, or G -equivariant, if

$$(f \circ \rho_G)(x) = (\rho_G \circ f)(x) \quad (\text{C.2})$$

for every x , i.e. if f commutes with the group action. If instead the action of G on either or both of \mathcal{X} and \mathcal{Y} , the definition extends to

- right-right equivariance:

$$f(x \cdot G) = f(x) \cdot G \quad (\text{C.3})$$

- right-left equivariance:

$$f(x \cdot G) = G^{-1} \cdot f(x) \quad (\text{C.4})$$

- left-right equivariance:

$$f(G \cdot x) = f(x) \cdot G^{-1} \quad (\text{C.5})$$

If any of (C.2)–(C.5) hold for all $G \in \mathcal{G}$, then we say f is equivariant to \mathcal{G} , or \mathcal{G} -equivariant.

Definition C.3 (Score Function). Given a time-dependent probability density $p_t(\phi)$ on \mathcal{F} , the *score function* at time t is the gradient (covector) field of the log-density:

$$\mathbf{s}(\phi, t) := \nabla_\phi \log p_t(\phi) \in T_\phi^* \mathcal{F}, \quad (\text{C.6})$$

where $T_\phi^* \mathcal{F}$ denotes the cotangent space at ϕ .

As a brief remark, we remind the reader that we focus on a single lattice site in this discussion for simplicity. We could easily generalize to a full, isotropic (and periodic) lattice $\mathbb{L} \cong \mathbb{T}^L \cong \mathbb{R}^L / \mathbb{Z}^L$, and view functions as being defined over product sets and product groups that cover the lattice. For instance, the score field defined over the full lattice would belong to the cotangent bundle $\mathbf{s} \in T^* \mathcal{F} = \bigsqcup_x T_\phi^* \mathcal{F}_x$.

Theorem C.4 (Transformation Law of the Score Function). *Let $G \in \mathcal{G}$ act smoothly on \mathcal{F} by $\phi \mapsto \phi' = \rho_G(\phi)$. If p_t is \mathcal{G} -invariant, then the score function transforms under the group action as*

$$\mathbf{s}'(\phi', t) = (D_\phi \rho_G)^{-\top} \mathbf{s}(\phi, t), \quad (\text{C.7})$$

where the Jacobian (differential) $D_\phi \rho_G := \partial \rho_G(\phi) / \partial \phi$ represents the linearization of the group action at ϕ .

Proof. By the chain rule for gradients on manifolds and assuming ρ_G is a diffeomorphism:

$$\mathbf{s}'(\phi', t) = \nabla_{\phi'} \log p_t(\phi') = \left(\frac{\partial \phi}{\partial \phi'} \right)^\top \nabla_\phi \log p_t(\phi), \quad (\text{C.8})$$

where we used invariance of the density: $p_t(\phi') = p_t(\phi)$. Since ρ_G is differentiable and invertible by assumption, we use the inverse function theorem to write

$$\frac{\partial\phi}{\partial\phi'} = \left(\frac{\partial\phi'}{\partial\phi}\right)^{-1}, \quad (\text{C.9})$$

and thus the general transformation law for the score function becomes

$$\mathbf{s}(\phi, t) \mapsto \mathbf{s}'(\phi', t) = \left(\frac{\partial\rho_G(\phi)}{\partial\phi}\right)^{-\top} \mathbf{s}(\phi, t), \quad (\text{C.10})$$

as desired. \square

This theorem shows that the score, as a gradient field, transforms like a covector (dual vector) under a change of variables induced by the symmetry group action. Its precise form depends on the nature of the field space and group action:

- **Linear representations:** If $\mathcal{F} = \mathbb{R}^n$ with $\rho_G(\phi) = R_G\phi$, then $D_\phi\rho_G = R_G$ and the score transforms by

$$\mathbf{s}' = (R_G)^{-\top} \mathbf{s},$$

e.g., for $\mathcal{G} = \mathbb{Z}_2$ acting by sign flip, $R_G = -\mathbb{1}$ so $\mathbf{s}' = -\mathbf{s}$.

- **Lie algebra-valued fields:** If $\phi \in \mathfrak{g}$ (the Lie algebra) and \mathcal{G} acts by the adjoint representation $\rho_G(\phi) = \text{Ad}_G\phi$, then $D_\phi\rho_G = \text{Ad}_G$, so

$$\mathbf{s}' = (\text{Ad}_G)^{-\top} \mathbf{s}.$$

- **Nonlinear group-valued fields:** If $\phi = U \in \mathcal{G}$ itself (e.g., lattice gauge links in $\text{SU}(N)$) with $\rho_G(U) = GUG^{-1}$ (conjugation), then the field space \mathcal{F} is the group manifold \mathcal{G} . The differential $D_U\rho_G$ gives the Jacobian acting on the tangent space $T_U\mathcal{G}$, and the score, as a cotangent vector, transforms via the dual action,

$$\mathbf{s}'(U') = (D_U\rho_G)^{-\top} \mathbf{s}(U),$$

reflecting covariance under the group's induced action on tangent spaces.

Some additional remarks:

- This result unifies all cases: the only difference lies in the Jacobian $D_\phi\rho_G$, which captures whether the group acts linearly (e.g., R_G) or nonlinearly (e.g., conjugation on \mathcal{G}).
- In curved manifolds, the Jacobian should be understood as the differential of the group action on the manifold, mapping tangent spaces.
- The theorem highlights that, under \mathcal{G} -invariance of the density, the score function is \mathcal{G} -equivariant in the appropriate sense: it transforms by the dual representation (contragredient) of the Jacobian of the group action.

C.2 Discussion on the U(1) Symmetry of Score Functions

Now, we present further discussion on the symmetries of the U(1) score function which are illuminating to understanding the transformation law for different representations.

We first work directly on the gauge group. Denote the score function at a lattice site x , viewed as a function of the gauge link U_μ for each μ , as

$$\mathbf{s}_\mu(x) = -\frac{\partial S[U]}{\partial U_\mu(x)}. \quad (\text{C.11})$$

In the group representation, link variables transform under the bi-regular representation of U(1) via

$$U_\mu(x) \mapsto U'_\mu(x) = \Omega(x)U_\mu(x)\Omega^\dagger(x + \hat{\mu}). \quad (\text{C.12})$$

In turn, the score function for the transformed variable can be computed using the chain rule:

$$\mathbf{s}'_\mu(x) = -\frac{\partial S[U']}{\partial U'_\mu(x)} = -\frac{\partial U_\mu(x)}{\partial U'_\mu(x)} \frac{\partial S[U]}{\partial U_\mu(x)}, \quad (\text{C.13})$$

where we assumed the action is gauge-invariant, i.e. $S[U'] = S[U]$. Since $U'_\mu(x) = \Omega^\dagger(x)U_\mu(x)\Omega(x + \hat{\mu})$, we can easily compute the Jacobian:

$$\frac{\partial U_\mu(x)}{\partial U'_\mu(x)} = \Omega^\dagger(x)\Omega(x + \hat{\mu}). \quad (\text{C.14})$$

Then, since U(1) is Abelian, we can write

$$\mathbf{s}'_\mu(x) = \Omega^\dagger(x)\mathbf{s}_\mu(x)\Omega(x + \hat{\mu}). \quad (\text{C.15})$$

Hence, in the group space, the score function transforms equivariantly under the bi-regular transformation.

Now we turn to the Lie algebra $\mathfrak{u}(1) \cong \mathbb{R}$ and consider the same argument in terms of angular variables, where we now redefine links as $U_\mu(x) \equiv e^{i\theta_\mu(x)}$ and gauge transformations as $\Omega(x) \equiv e^{i\omega(x)}$. Now, we view the score as a function of the real valued link phases $\theta_\mu(x) \in [-\pi, \pi)$ and denote

$$\mathbf{s}_\mu(x) := -\frac{\partial S[\theta]}{\partial \theta_\mu(x)}. \quad (\text{C.16})$$

The link phases transform under the group as a linear shift:

$$\theta_\mu(x) \mapsto \theta'_\mu(x) = \theta_\mu(x) + \omega(x) - \omega(x + \hat{\mu}), \quad (\text{C.17})$$

which can be seen as a discretized version of how the Abelian gauge field transforms:

$$A_\mu(x) \mapsto A'_\mu(x) = A_\mu(x) - \partial_\mu \varphi(x). \quad (\text{C.18})$$

Once again, the score function obeys a transformation law via the chain rule:

$$\mathbf{s}'_\mu(x) = \frac{\partial \theta_\mu(x)}{\partial \theta'_\mu(x)} \mathbf{s}_\mu(x). \quad (\text{C.19})$$

But since the group action in the algebra is by affine translation, the Jacobian is simply the identity, meaning that, when expressed as a function of angular variables in the Lie algebra, the score is gauge-invariant. In other words, the score function transforms under the adjoint representation, which is trivial for U(1).

References

- [1] N. Metropolis, A. W. Rosenbluth, M. N. Rosenbluth, A. H. Teller, and E. Teller. *Equation of State Calculations by Fast Computing Machines*. *J. Chem. Phys.* **21** (1953) 1087–1092.
- [2] S. Duane, A. D. Kennedy, B. J. Pendleton, and D. Roweth. *Hybrid Monte Carlo*. *Phys. Lett. B* **195** (1987) 216–222.
- [3] S. Gupta. *Hybrid Monte Carlo Simulations of a Two-Dimensional Gauge Theory*. *Phys. Lett. B* **278** (1992) 317–322.
- [4] A. D. Kennedy and K. M. Bitar. *An Exact Local Hybrid Monte Carlo Algorithm for Gauge Theories*. *Nucl. Phys. B Proc. Suppl.* **34** (1994) 786–788 [[hep-lat/9311017](#)].
- [5] U. Wolff, *Critical Slowing Down*, *Nucl. Phys. B Proc. Suppl.* **17** (1990) 93–102.
- [6] K. G. Wilson. *Confinement of Quarks*. *Phys. Rev. D* **10** (1974) 2445–2459.
- [7] R. Fantoni and J. R. Klauder. *Monte Carlo Evaluation of the Continuum Limit of the Two-Point Function of Two Euclidean Higgs Real Scalar Fields Subject to Affine Quantization*. *Phys. Rev. D* **104** (2021) 054514 [[2107.08601](#)].
- [8] D. Albandea, P. Hernández, A. Ramos, and F. Romero-López. *Improved Topological Sampling for Lattice Gauge Theories*. *PoS LATTICE2021* (2022) 183 [[2111.05745](#)].
- [9] G. O. Roberts and R. L. Tweedie. *Exponential Convergence of Langevin Distributions and Their Discrete Approximations*. *Bernoulli* **2**(4) (1996) 341–363.
- [10] J. Kotze. *Introduction to Monte Carlo Methods for an Ising Model of a Ferromagnet*. [arXiv:0803.0217](#).
- [11] D. Rezende and S. Mohamed. *Variational Inference with Normalizing Flows*. *Proc. 32nd Int. Conf. on Machine Learning. PMLR* **37** (2015) 1530–1538 [[1505.05770](#)].
- [12] L. Dinh, J. Sohl-Dickstein and S. Bengio. *Density Estimation Using Real NVP*. [arXiv:1605.08803](#).
- [13] G. Papamakarios, E. Nalisnick, D. J. Rezende, S. Mohamed, and B. Lakshminarayanan. *Normalizing Flows for Probabilistic Modeling and Inference*. *J. Mach. Learn. Res.* **22** (2021) 57:2617–57:2680 [[1912.02762](#)].
- [14] R. T. Q. Chen, Y. Rubanova, J. Bettencourt, D. Duvenaud. *Neural Ordinary Differential Equations*. *Proc. 32nd Int. Conf. on Neural Information Processing Systems (NeurIPS 2018)* (2018) 6572–6583 [[1806.07366](#)].
- [15] M. S. Albergo, G. Kanwar, and P. E. Shanahan. *Flow-Based Generative Models for Markov Chain Monte Carlo in Lattice Field Theory*. *Phys. Rev. D* **100**(3) (2019) 034515 [[arXiv:1904.12072](#)].

- [16] D. J. Rezende, G. Papamakarios, S. Racanière, M. S. Albergo, G. Kanwar, P. E. Shanahan, and K. Cranmer. *Normalizing Flows on Tori and Spheres*. [Proceedings of the 37th International Conference on Machine Learning \(ICML 2020\)](#), *PMLR* **119** (2020) 8083–8092 [[2002.02428](#)].
- [17] G. Kanwar, M. S. Albergo, D. Boyda, K. Cranmer, D. C. Hackett, S. Racanière, D. J. Rezende, and P. E. Shanahan. *Equivariant Flow-Based Sampling for Lattice Gauge Theory*. *Phys. Rev. Lett.* **125** (2020) 121601 [[2003.06413](#)].
- [18] D. Boyda, G. Kanwar, S. Racanière, D. J. Rezende, M. S. Albergo, K. Cranmer, D. C. Hackett, P. E. Shanahan. *Sampling Using $SU(N)$ Gauge Equivariant Flows*. *Phys. Rev. D* **103** (2021) 074504 [[2008.05456](#)].
- [19] M. S. Albergo, D. Boyda, D. C. Hackett, G. Kanwar, K. Cranmer, S. Racanière, D. J. Rezende, and P. E. Shanahan. *Introduction to Normalizing Flows for Lattice Field Theory*. [arXiv:2101.08176](#).
- [20] M. S. Albergo, D. Boyda, K. Cranmer, D. C. Hackett, G. Kanwar, S. Racanière, D. J. Rezende, F. Romero-López, P. E. Shanahan, and J. M. Urban. *Flow-Based Sampling in the Lattice Schwinger Model at Criticality*. *Phys. Rev. D* **106** (2022) 014514 [[2202.11712](#)].
- [21] R. Abbott, M. S. Albergo, D. Boyda, K. Cranmer, D. C. Hackett, G. Kanwar, S. Racanière, D. J. Rezende, F. Romero-López, P. E. Shanahan, B. Tian, J. M. Urban. *Gauge-Equivariant Flow Models for Sampling in Lattice Field Theories with Pseudofermions*. *Phys. Rev. D* **106** (2022) 074506 [[2207.08945](#)].
- [22] R. Abbott, M. S. Albergo, A. Botev, D. Boyda, K. Cranmer, D. C. Hackett, G. Kanwar, A. G. D. G. Matthews, S. Racanière, A. Razavi, D. J. Rezende, F. Romero-López, P. E. Shanahan, and J. M. Urban. *Sampling QCD Field Configurations with Gauge-Equivariant Flow Models*. *PoS LATTICE2022* (2023) 036 [[2208.03832](#)].
- [23] R. Abbott, M. S. Albergo, A. Botev, D. Boyda, K. Cranmer, D. C. Hackett, A. G. D. G. Matthews, S. Racanière, A. Razavi, D. J. Rezende, F. Romero-López, P. E. Shanahan, and J. M. Urban. *Aspects of Scaling and Scalability for Flow-Based Sampling of Lattice QCD*. *Eur. Phys. J. A* **59** (2023) 257 [[2211.07541](#)].
- [24] R. Abbott, M. S. Albergo, D. Boyda, D. C. Hackett, G. Kanwar, F. Romero-López, P. E. Shanahan, and J. M. Urban. *Multiscale Normalizing Flows for Gauge Theories*. *PoS LATTICE2023* (2024) 035 [[2404.10819](#)].
- [25] R. Abbott, D. Boyda, G. Kanwar, F. Romero-López, D. C. Hackett, P. E. Shanahan, and J. M. Urban. *Progress in Normalizing Flows for 4d Gauge Theories*. *PoS LATTICE2024* (2025) 066 [[2502.00263](#)].
- [26] L. Del Debbio, J. M. Rossney, and M. Wilson. *Efficient Modeling of Trivializing Maps for Lattice ϕ^4 Theory Using Normalizing Flows: A First Look at Scalability*. *Phys. Rev. D* **104** (2021) 094507 [[2105.12481](#)].
- [27] A. Bulgarelli, E. Cellini, and A. Nada. *Scaling of Stochastic Normalizing Flows in $SU(3)$ Lattice Gauge Theory*. *Phys. Rev. D* **111** (2025) 074517 [[2412.00200](#)].

- [28] J. Komijani and M. K. Marinkovic. *Generative Models for Scalar Field Theories: How to Deal with Poor Scaling?* *PoS LATTICE2022* (2023) 019 [[2301.01504](#)].
- [29] D. Boyda, S. Calì, S. Foreman, L. Funcke, D. C. Hackett, Y. Lin, G. Aarts, A. Alexandru, X.-Y. Jin, B. Lucini, and P. E. Shanahan. *Applications of Machine Learning to Lattice Quantum Field Theory. Snowmass 2021* (2022) 2 [[2202.05838](#)].
- [30] S. Lawrence. *Machine-Learning Approaches to Accelerating Lattice Simulations*, *PoS LATTICE2024* (2025) 010 [[2502.02670](#)].
- [31] F. Noé, S. Olsson, J. Köhler, H. Wu. *Boltzmann Generators: Sampling Equilibrium States of Many-Body Systems with Deep Learning*. *Science* **365** (2019) eaaw1147 [[1812.01729](#)].
- [32] A. Vaswani, N. Shazeer, N. Parmar, J. Uszkoreit, L. Jones, A. N. Gomez, L. Kaiser, and I. Polosukhin. *Attention Is All You Need*. *Proceedings of the 31st International Conference on Neural Information Processing Systems (NeurIPS 2017)* **30** (2017) [[1706.03762](#)].
- [33] M. Tancik, P. P. Srinivasan, B. Mildenhall, S. Fridovich-Keil, N. Raghavan, U. Singhal, R. Ramamoorthi, J. T. Barron, and R. Ng. *Fourier Features Let Networks Learn High Frequency Functions in Low Dimensional Domains*. *Adv. Neural Inf. Process. Syst.* **33** (2020) 7537–7547 [[2006.10739](#)].
- [34] O. Ronneberger, P. Fischer, and T. Brox. *U-Net: Convolutional Networks for Biomedical Image Segmentation*. *Proc. MICCAI 2015*, Springer (2015) 234–241 [[1505.04597](#)].
- [35] D. P. Kingma and M. Welling. *Auto-Encoding Variational Bayes*. *Proc. 2nd International Conference on Learning Representations (ICLR 2014)* [[1312.6114](#)].
- [36] D. P. Kingma and J. Ba. *Adam: A Method for Stochastic Optimization*. *3rd International Conference on Learning Representations (ICLR 2015)* [[1412.6980](#)].
- [37] I. Goodfellow, J. Pouget-Abadie, M. Mirza, B. Xu, D. Warde-Farley, S. Ozair, A. Courville, and Y. Bengio. *Generative Adversarial Nets*. *Advances in Neural Information Processing Systems* **27** (2014) 2672–2680 [[1406.2661](#)].
- [38] P. Vincent. *A Connection Between Score Matching and Denoising Autoencoders*. *Neural Computation* **23** (2011) 1661–1674.
- [39] J. Sohl-Dickstein, E. Weiss, N. Maheswaranathan, and S. Ganguli. *Deep Unsupervised Learning Using Nonequilibrium Thermodynamics*. *Proceedings of the 32nd International Conference on Machine Learning (ICML 2015)*, *PMLR* **37** (2015) 2256–2265 [[1503.03585](#)].
- [40] J. Ho, A. Jain, and P. Abbeel. *Denoising Diffusion Probabilistic Models*. *Proceedings of the 34th International Conference on Neural Information Processing Systems (NeurIPS 2020)* **574** (2020) 6840–6851 [[2006.11239](#)].
- [41] A. Hyvärinen. *Estimation of Non-Normalized Statistical Models by Score Matching*. *J. Mach. Learn. Res.* **6** (2005) 695–709.

- [42] S. Kullback and R. A. Leibler. *On Information and Sufficiency*. *Ann. Math. Stat.* **22** (1951) 79–86.
- [43] Y. Song and S. Ermon. *Generative Modeling by Estimating Gradients of the Data Distribution*. *Proceedings of the 33rd Conference on Neural Information Processing Systems (NeurIPS 2019)* **1076** (2019) 11918–11930 [[1907.05600](#)].
- [44] Y. Song, J. Sohl-Dickstein, D. P. Kingma, A. Kumar, S. Ermon, and B. Poole. *Score-Based Generative Modeling through Stochastic Differential Equations*. *9th International Conference on Learning Representations (ICLR 2021)* [[2011.13456](#)].
- [45] L. Yang, Z. Zhang, Y. Song, S. Hong, R. Xu, Y. Zhao, W. Zhang, B. Cui, and M.-H. Yang. *Diffusion Models: A Comprehensive Survey of Methods and Applications*. *ACM Comput. Surv.* **56** (2023) 105:1–105:39 [[2209.00796](#)].
- [46] T. Karras, M. Aittala, S. Laine, and T. Aila, *Elucidating the Design Space of Diffusion-Based Generative Models*. *Adv. Neural Inf. Process. Syst.* **35** (2022) 26565–26577 [[2206.00364](#)].
- [47] T. Dockhorn, A. Vahdat, and K. Kreis. *Score-Based Generative Modeling with Critically-Damped Langevin Diffusion*. *arXiv:2112.07068*.
- [48] A. Jolicoeur-Martineau, R. Piché-Taillefer, R. T. des Combes, and I. Mitliagkas. *Adversarial Score Matching and Improved Sampling for Image Generation*. *arXiv:2009.05475*.
- [49] A. Jolicoeur-Martineau, K. Li, R. Piché-Taillefer, T. Kachman, and I. Mitliagkas, *Gotta Go Fast When Generating Data with Score-Based Models*. *arXiv:2105.14080*.
- [50] F.-A. Croitoru, V. Hondru, R. T. Ionescu, and M. Shah. *Diffusion Models in Vision: A Survey*. *IEEE Trans. Pattern Anal. Mach. Intell.* **45**(9) (2023) 10850–10869. [[2209.04747](#)].
- [51] C. Saharia, W. Chan, S. Saxena, L. Lit, J. Whang, E. Denton, S. K. S. Ghasemipour, B. K. Ayan, S. S. Mahdavi, R. Gontijo-Lopes, T. Salimans, J. Ho, D. J. Fleet, and M. Norouzi. *Photorealistic Text-to-Image Diffusion Models with Deep Language Understanding*. *Proc. 36th Int. Conf. Neural Information Processing Systems (NeurIPS 2022)* (2022) 36479–36494. [[2205.11487](#)].
- [52] A. Q. Nichol, P. Dhariwal, A. Ramesh, P. Shyam, P. Mishkin, B. McGrew, I. Sutskever, and M. Chen. *GLIDE: Towards Photorealistic Image Generation and Editing with Text-Guided Diffusion Models*. *Proc. 39th Int. Conf. Mach. Learn. (ICML)* (2022) 16784–16804. [[2112.10741](#)].
- [53] R. Rombach, A. Blattmann, D. Lorenz, P. Esser, and B. Ommer. *High-Resolution Image Synthesis with Latent Diffusion Models*. *Proc. IEEE/CVF Conf. Comput. Vis. Pattern Recognit. (CVPR)* (2022) 10674–10685. [[2112.10752](#)].
- [54] A. Ramesh, P. Dhariwal, A. Nichol, C. Chu, and M. Chen. *Hierarchical Text-Conditional Image Generation with CLIP Latents*. *2204.06125* (2022).
- [55] C. Pang, J. Qiao, X. Zeng, Q. Zou, and L. Wei. *Deep Generative Models in De Novo Drug Molecule Generation*. *J. Chem. Inf. Model.* **64**(7) (2024) 2174–2194.

- [56] A. Alakhdar, B. Poczos, and N. Washburn. *Diffusion Models in De Novo Drug Design*. *J. Chem. Inf. Model.* **64**(19) (2024) 7238–7256.
- [57] J. L. Watson, D. Juergens, N. R. Bennett, B. L. Trippe, J. Yim, H. E. Eisenach, W. Ahern, A. J. Borst, R. J. Ragotte, L. F. Milles, B. I. M. Wicky, N. Hanikel, S. J. Pellock, A. Courbet, W. Sheffler, J. Wang, P. Venkatesh, I. Sappington, S. V. Torres, A. Lauko, V. De Bortoli, E. Mathieu, S. Ovchinnikov, R. Barzilay, T. S. Jaakkola, F. DiMaio, M. Baek, and D. Baker. *De Novo Design of Protein Structure and Function with RFdiffusion*. *Nature* **620**(7976) (2023) 1089–1100.
- [58] M. Sako, N. Yasuo, and M. Sekijima. *DiffInt: A Diffusion Model for Structure-Based Drug Design with Explicit Hydrogen Bond Interaction Guidance*. *J. Chem. Inf. Model.* **65**(1) (2025) 71–82.
- [59] G. Corso, H. Stärk, B. Jing, R. Barzilay, and T. S. Jaakkola. *DiffDock: Diffusion Steps, Twists, and Turns for Molecular Docking*. *Proc. 11th Int. Conf. Learn. Represent. (ICLR)* (2023). [[arXiv:2210.01776](https://arxiv.org/abs/2210.01776)].
- [60] A. D. Fokker. *Die mittlere Energie rotierender elektrischer Dipole im Strahlungsfeld*. *Ann. Phys.* **348** (1914) 810–820.
- [61] M. Planck. *Über einen Satz der statistischen Dynamik und seine Erweiterung in der Quantentheorie*. *Sitzungsberichte der Preussischen Akademie der Wissenschaften zu Berlin* **24** (1917) 324–341.
- [62] P. Langevin. *Sur la théorie du mouvement brownien [On the Theory of Brownian Motion]*. *C. R. Acad. Sci. Paris.* **146** (1908) 530–533.
- [63] B. D. O. Anderson. *Reverse-Time Diffusion Equation Models*. *Stochastic Processes and their Applications* **12** (1982) 313–326.
- [64] C. Runge. *Ueber die numerische Auflösung von Differentialgleichungen*. *Math. Ann.* **46** (1895) 167–178.
- [65] W. Kutta. *Beitrag zur näherungsweise Integration totaler Differentialgleichungen*. *Z. Math. Phys.* **46** (1901) 435–453.
- [66] R. W. Hamming. *Stable Predictor-Corrector Methods for Ordinary Differential Equations*. *J. ACM* **6** (1959) 37–47.
- [67] L. Wang, G. Aarts, and K. Zhou, *Generative Diffusion Models for Lattice Field Theory*. [arXiv:2311.03578](https://arxiv.org/abs/2311.03578).
- [68] L. Wang, G. Aarts, and K. Zhou, *Diffusion Models as Stochastic Quantization in Lattice Field Theory*. *J. High Energy Phys.* **5** (2024) 60 [[2309.17082](https://arxiv.org/abs/2309.17082)].
- [69] G. Aarts, L. Wang, and K. Zhou, *Diffusion Models and Stochastic Quantisation in Lattice Field Theory*. *PoS LATTICE2024* (2025) 037 [[2412.13704](https://arxiv.org/abs/2412.13704)].
- [70] Q. Zhu, G. Aarts, W. Wang, K. Zhou, and L. Wang, *Diffusion Models for Lattice Gauge Field Simulations*. [arXiv:2410.19602](https://arxiv.org/abs/2410.19602).

- [71] D. E. Habibi, G. Aarts, L. Wang, and K. Zhou, *Diffusion Models Learn Distributions Generated by Complex Langevin Dynamics*, *PoS LATTICE2024* (2025) 039 [[2412.01919](#)].
- [72] L. Del Debbio, L. Giusti, and C. Pica. *Topological Susceptibility in the $SU(3)$ Gauge Theory*. *Phys. Rev. Lett.* **94** (2005) 032003 [[hep-th/0407052](#)].
- [73] M. Lüscher and F. Palombi. *Universality of the Topological Susceptibility in the $SU(3)$ Gauge Theory*. *JHEP* **09** (2010) 110 [[1008.0732](#)].
- [74] M. Cè, C. Consonni, G. P. Engel, and L. Giusti. *Non-Gaussianities in the Topological Charge Distribution of the $SU(3)$ Yang–Mills Theory*. *Phys. Rev. D* **92** (2015) 074502 [[1506.06052](#)].
- [75] M. Cè, M. García Vera, L. Giusti, and S. Schaefer. *The Topological Susceptibility in the Large- N Limit of $SU(N)$ Yang–Mills Theory*. *Phys. Lett. B* **762** (2016) 232–236 [[1607.05939](#)].
- [76] A. Athenodorou, C. Bonanno, C. Bonati, G. Clemente, F. D’Angelo, M. D’Elia, L. Maio, G. Martinelli, F. Sanfilippo, and A. Todaro. *Topological Susceptibility of $N_f = 2 + 1$ QCD from Staggered Fermion Spectral Projectors at High Temperatures*. *JHEP* **10** (2022) 197 [[2208.08921](#)].
- [77] Q. Zhu, G. Aarts, W. Wang, K. Zhou, and L. Wang, *Physics-Conditioned Diffusion Models for Lattice Gauge Theory*. [arXiv:2502.05504](#).
- [78] P. H. Damgaard, H. Huffel. *Stochastic Quantization*. *Phys. Rept.* **152** (1987) 227.
- [79] C. Gattringer and C. Lang. *Quantum Chromodynamics on the Lattice: An Introductory Presentation*. *Lecture Notes in Physics* **788**, Springer Berlin, Heidelberg (2010).
- [80] I. Montvay and G. Münster. *Quantum Fields on a Lattice*. *Cambridge Monographs on Mathematical Physics*, Cambridge University Press, Cambridge (1994).
- [81] J. Smit. *Introduction to Quantum Fields on a Lattice*. *Cambridge Lecture Notes in Physics* **15**, Cambridge University Press, Cambridge (2002).
- [82] R. P. Feynman. *The Principle of Least Action in Quantum Mechanics*. *Ph.D. thesis, Princeton U.* (1942).
- [83] K. Binder, *Critical Properties from Monte Carlo Coarse Graining and Renormalization*. *Phys. Rev. Lett.* **47** (1981) 693–696.
- [84] J. Zinn-Justin. *Quantum Field Theory and Critical Phenomena: Fifth Edition*. *International Series of Monographs in Physics* **77**, Oxford University Press, Oxford (2021).
- [85] M. E. Peskin. *An Introduction to Quantum Field Theory*. Addison-Wesley, Reading (1995). [doi:10.1201/9780429503559](#).
- [86] M. Lüscher. *Topology of Lattice Gauge Fields*. *Commun. Math. Phys.* **85** (1982) 39–48.

- [87] J. Polonyi. *Topological Charge in Lattice Gauge Theory*. *Prog. Math. Phys.* **8** (1983) 168–180.
- [88] B. Alles, G. Boyd, M. D’Elia, A. Di Giacomo, and E. Vicari. *Hybrid Monte Carlo and Topological Modes of Full QCD*. *Phys. Lett. B* **389** (1996) 107–111 [[hep-lat/9607049](#)].
- [89] J. Skilling. *The Eigenvalues of Mega-dimensional Matrices*, in *Maximum Entropy and Bayesian Methods: Cambridge, England, 1988*. *Fundamental Theories of Physics* **36**, Springer Netherlands, Dordrecht (1989) 455–466.
- [90] M. F. Hutchinson, *A Stochastic Estimator of the Trace of the Influence Matrix for Laplacian Smoothing Splines*. *Commun. Stat. Simul. Comput.* **18** (1989) 3, 1059–1076.
- [91] P. Hitczenko and S. Kwapien. *On the Rademacher Series*. *Probability in Banach Spaces* **9** (1994) 31–36.
- [92] ALPHA Collaboration, U. Wolff. *Monte Carlo Errors with Less Errors*. *Comput. Phys. Commun.* **156** (2004) 143–153 [[hep-lat/0306017](#)].
- [93] A. Paszke, S. Gross, F. Massa, A. Lerer, J. Bradbury, G. Chanan, T. Killeen, Z. Lin, N. Gimelshein, L. Antiga, A. Desmaison, A. Kopf, E. Yang, Z. DeVito, M. Raison, A. Tejani, S. Chilamkurthy, B. Steiner, L. Fang, J. Bai, and S. Chintala. *PyTorch: An Imperative Style, High-Performance Deep Learning Library*. *Proceedings of the 33rd Annual Conference on Neural Information Processing Systems (NeurIPS 2019)* **721** (2019) 8024–8035 [[1912.01703](#)].
- [94] C. R. Harris, K. J. Millman, S. J. van der Walt, R. Gommers, P. Virtanen, D. Cournapeau, E. Wieser, J. Taylor, S. Berg, N. J. Smith, R. Kern, M. Picus, S. Hoyer, M. H. van Kerkwijk, M. Brett, A. Haldane, J. F. del Río, M. Wiebe, P. Peterson, P. Gérard-Marchant, K. Sheppard, T. Reddy, W. Weckesser, H. Abbasi, C. Gohlke, and T. E. Oliphant. *Array Programming with NumPy*. *Nature* **585** (2020) 357–362 [[2006.10256](#)].
- [95] P. Virtanen, R. Gommers, T. E. Oliphant, M. Haberland, T. Reddy, D. Cournapeau, E. Burovski, P. Peterson, W. Weckesser, J. Bright, S. J. van der Walt, M. Brett, J. Wilson, K. J. Millman, N. Mayorov, A. R. J. Nelson, E. Jones, R. Kern, E. Larson, C. J. Carey, Í. Polat, Y. Feng, E. W. Moore, J. VanderPlas, D. Laxalde, J. Perktold, R. Cimrman, I. Henriksen, E. A. Quintero, C. R. Harris, A. M. Archibald, A. H. Ribeiro, F. Pedregosa, and P. van Mulbregt. *SciPy 1.0: Fundamental Algorithms for Scientific Computing in Python*. *Nat. Methods* **17** (2020) 261–272 [[1907.10121](#)].
- [96] J. D. Hunter. *Matplotlib: A 2D Graphics Environment*. *Computing in Science and Engineering* **9** (2007) 90–95.
- [97] Adobe Inc. *Adobe Illustrator, Version 23.0.3*, 2019.